This is to certify that the
thesis entitled

DIESEL COMBUSTION AND FUEL SPRAY ANALYSIS USING AN
OPTICAL ENINGE WITH PRESSURE DIAGNOSTICS, INFRARED
THERMOGRAPHY, AND HIGH-SPEED PHOTGRAPHY

presented by

Cody William Squibb

has been accepted towards fulfillment
of the requirements for the

___M.S.___   degree in   ___Mechanical Engineering___

_____
Major Professor's Signature

_____5/14/09_____
Date

PLACE IN RETURN BOX to remove this checkout from your record.
TO AVOID FINES return on or before date due.
MAY BE RECALLED with earlier due date if requested.

DATE DUE	DATE DUE	DATE DUE

DIESEL COMBUSTION AND FUEL SPRAY ANALYSIS USING AN OPTICAL
ENGINE WITH PRESSURE DIAGNOSTICS, INFRARED THERMOGRAPHY, AND
HIGH-SPEED PHOTGRAPHY

By

Cody William Squibb

A THESIS

Submitted to
Michigan State University
in partial fulfillment of the requirements
for the degree of

MASTER OF SCIENCE

Mechanical Engineering

2009

ABSTRACT

DIESEL COMBUSTION AND FUEL SPRAY ANALYSIS USING AN OPTICAL ENGINE WITH PRESSURE DIAGNOSTICS, INFRARED THERMOGRAPHY, AND HIGH-SPEED PHOTGRAPHY

By

Cody William Squibb

Infrared and high-speed images along with pressure information have been recorded and used to evaluate events inside an optically accessible Diesel engine. A 6- and a 14-hole nozzle are examined, each at two load conditions. The fuel spray and combustion characteristics are examined and discussed. It is determined from examination of the fuel sprays that the 6-hole nozzle penetrates the combustion bowl more quickly but the 14-hole nozzle tends to distribute fuel more uniformly. Comparison of the images recorded from in-cylinder combustion experiments with pressure data demonstrated the differences in performance between the two nozzles. Infrared photography showed a start of combustion earlier than was seen in the high-speed pictures; pressure data showed start of combustion earlier than was captured by either camera. High-speed photography showed a possible increase in soot production for the 6-hole nozzle as compared to the 14-hole nozzle. In-cylinder temperatures were estimated from infrared pictures. Overall, higher pressures and estimated temperatures were produced with the 6-hole nozzle while the 14-hole nozzle tended to reduce visible soot while yielding higher IMEP values for these operating conditions. This presentation describes the physics behind these observations, the experimental methods developed for this effort, and the performance of these two combustion systems.

ACKNOWLEDGEMENTS

TABLE OF CONTENTS

LIST OF TABLES

Images in this Thesis are presented in color.

LIST OF FIGURES

KEY TO SYMBOLS AND ABBREVIATIONS

ATDC	After Top Dead Center
BTDC	Before Top Dead Center
C_1, C_2	Planck's Constants
CAD	Crank Angle Degree
fps	Frames Per Second
HRR	Heat Release Rate
MFB	Mass Fraction Burned
IMEP	Indicated Mean Effective Pressure
RPM	Revolution Per Minute
SOC	Start of Combustion
T	Temperature
TDC	Top Dead Center
b	Blackbody
I	Intensity
ε	Emissivity
λ	Wavelength
f	Function of
f_b	Blackbody Function
τ	Transmissivity
σ	Stefan-Boltzmann Constant
atm	Atmosphere
°C	Degrees Celsius

°F	Degrees Fahrenheit
Hz	Hertz
mg	Milligrams
mm	Millimeters
ms	milliseconds
pC	Picocoulomb

CHAPTER 1

INTRODUCTION AND BACKGROUND

Information regarding the events within an optical Diesel engine has been acquired using infrared thermography, high-speed photography, and in-cylinder pressure data. A high-speed camera was utilized such that the combustion and fuel spray events could be seen in the same cycle. An infrared camera was calibrated for temperatures, while taking into account several important aspects. The in-cylinder pressure data were also extremely important for analysis. When used in conjunction with each other, these techniques lead to information that is not easily achieved through other means.

Infrared, high-speed, and pressure techniques can be used to gather information about Diesel engines. There are certain distinct advantages in using infrared techniques to gather information about a Diesel engine. When applied to fuel spray, the fuel vapors that are nearly transparent in the visible light range are clearly defined in the infrared range. This allows for a more detailed analysis of fuel mixing and fuel spray quality. There are certain drawbacks, however. Air and other gases do not emit readily in the infrared range. Therefore, determination of the temperature of the hot gases outside the fuel plume is nearly impossible with this technique. Also, for this particular application, some energy is lost due to transmission losses. High-speed photography can likewise be used to gather photographical information inside the engine cylinder. High-speed photography allows for many more images to be acquired per cycle in order to achieve greater insight into individual cycles. Pressure data can also be utilized for analysis of engine cycles. These

data can be used to evaluate performance parameters of the engine. A large amount of information is gained by using these methods of analysis.

1.1 Infrared Imaging Techniques

The use of infrared cameras to gather information about a Diesel engine has many benefits and some shortfalls. Some substances that are not easily seen in the visible light range are easily seen in the infrared range. In particular, fuel vapor and exothermic reactions are better viewed in the infrared region. The use of infrared techniques also allows for estimation of in-cylinder temperatures. A main shortfall of current infrared technology is the speed of infrared imaging only allows for the capture of one picture per combustion or fuel spray event at the engine speeds experienced in these experiments.

1.1.1 Infrared Thermography

In order to interpret infrared data, one must understand the basics of infrared thermography. Infrared thermography is the process of inferring the temperature of an object by measuring the intensity of the electromagnetic waves emitted by the object and captured by an infrared camera. In this application, infrared thermography is used to estimate the in-cylinder temperature field during combustion events.

It is first necessary to understand some basics of infrared radiation. The infrared spectrum lies between the visible and microwave ranges from the wavelengths of 750 μm to 1 mm. The electromagnetic waves found in this range transmit heat. The amount of radiation, and hence, the heat transfer, depends on the temperature of the object and

certain properties of the object. This radiation is acquired by different bodies, in this case, an infrared camera.

Radiation can be transmitted, emitted, absorbed, or reflected. The transmission and emission of energy is of particular importance to this application. Transmissivity is defined as the amount of radiation transmitted through an object (such as, in this case, a piston window) divided by the amount of incident radiation. The value of transmissivity will be a value between 0 and 1, with a value of 1 meaning that all of the radiation is transmitted through the substance and 0 meaning the substance is completely opaque. Emissivity is defined as the amount of energy emitted by an object divided by the ideal amount of radiation emitted at that temperature. An object that is a perfect emitter is called a blackbody emitter and has an emissivity value of 1. This means that the object emits radiation perfectly according to Planck's Law. Planck's Law describes the amount of radiation per surface area given off by a blackbody as a function of wavelength and temperature. Real substances deviate from this curve, having emissivity values less than 1 and are deemed "gray" bodies. It is also dictated from this relationship that as the temperature of an object increases, the object will emit more radiation. Knowing this, one can tell the temperature of a blackbody by using a device that samples a segment of wavelengths and finds the amount of energy emitted. By using an infrared camera, a device that turns the absorbed energy from an object into voltage, it is possible to estimate temperature using a calibration to this voltage.

In order to attain an equation for the total radiation intensity along a line-of-sight, such as in this case, a line integration approach must be used. The radiation intensity is defined as the radiative energy flow per time per area per unit solid angle. The line

3

integration approach assumes that the substances viewed are optically thin. This is usually a valid assumption for hot gases, due to the limited amount of radiation coming from them and the optical properties inherent to gases. This form assumes limited interference and radiation from the camera. Radiation intensity, I, for any object at any wavelength can be found using Planck's Law, given by

$$I_\lambda = \varepsilon_\lambda I_{b,\lambda} = \varepsilon_\lambda \frac{2\pi C_1}{\lambda^5 (e^{C_2/\lambda T} - 1)}$$ (1)

where λ is the wavelength , ε_λ is the emissivity of the object at a wavelength, C_1 and C_2 are radiation constants of Plank's law, and T is the temperature of the object. Assuming a constant emissivity, $\bar{\varepsilon}$, and integrating over the entire spectrum yields

$$I_{engine} = \bar{\varepsilon}\frac{\sigma T^4}{\pi}$$ (2)

where σ is the Stefan-Boltzmann constant. The pi term of the denominator comes from solid angle integration. However, this form must be corrected for the region of interest, namely the 3-5 micron wavelength range seen by the camera. Values are tabulated as a function of temperature and wavelength for the radiative power. This gives the intensity of a gray body in this wavelength range of the form

$$I_{engine} = [f(\lambda_2 T) - f(\lambda_1 T)]\varepsilon\sigma T^4$$ (3)

Another object to take into account is the effect of the sapphire window. The transmissivity of the window will decrease the energy acquired by the camera as

$$I_{camera} = \tau_{window} I_{engine} = \tau_{window}[f_b(\lambda_2 T) - f_b\lambda_1 T)]\varepsilon\sigma T^4$$ (4)

That is, the window will decrease the energy seen by the camera by the transmissivity value.

Using gray body approximations, there will be three possible causes of radiation inside the combustion chamber. The total intensity will then be the sum of these. The first is radiation emitted from the hot gases in the combustion chamber directly to the camera. The second source of radiation will be radiation emitted by the background and attenuated through the gases. Calculation of the transmissivity, τ_{mix}, of the gases is then required, given by

$$\tau_{mix} = 1 - \varepsilon_{mix} \qquad (5)$$

since there is insignificant absorption or reflection by the gas. The third source comes from the radiation of the hot gases reflected by the background and then attenuated by the gas. This source requires calculation of the reflectivity of the background, $\rho_{background}$, given by

$$\rho_{background} = 1 - \varepsilon_{background} \qquad (6)$$

due to the lack of absorption or transmission by the background. The total intensity can then be expressed as

$$I_{engine} = \varepsilon_{mix} I_{b,mix} + \varepsilon_{background} \tau_{mix} I_{b,background} + \rho_{background} \tau_{mix} I_{b,mix} \qquad (7)$$

Substitution yields

$$I_{engine} = \varepsilon_{mix} I_{b,mix} + \varepsilon_{background} (1 - \varepsilon_{mix}) I_{b,background} + (1 - \varepsilon_{background}) (1 - \varepsilon_{mix}) I_{b,mix} \qquad (8)$$

This equation can then be used to find the total radiative intensity seen by the camera.

Due to the complexity and lack of accuracy in modeling of the mixture inside the engine cylinder, a more direct approach was taken to calibrate the camera for

temperature, thereby simplifying equation (8). When calibrating using the camera, wavelength effects are accounted for inherently with the camera. By calibrating the camera with a flame that has a similar emissivity to those of the mixtures inside the engine, the mixture emissivity terms are accounted for. Likewise, placing a sapphire window with a similar transmissivity to the piston window in the cameras view will eliminate the transmissivity effect of the piston window. Correcting for the neutral density filter used was accomplished by installing the filter when creating the correction file, thereby eliminating any effects from this. Assuming background effects are negligible eliminates these effects. This is appropriate as, at higher temperatures, the background effects of the cylinder head are minor compared to emissivity estimations. This calibration process creates a correction file which relates the intensity only as a function of temperature as

$$I_{camera} = f(T^4) \tag{9}$$

This equation yields a built in function which can return a temperature for a particular intensity reading of the camera. The implementation of the calibration file is accomplished with the software supplied with the infrared camera.

Emissivity and concentration play a large role in the amount of energy captured by the infrared camera. The emissivity of a flame is a varying parameter that changes rapidly both globally and locally. It has been found that the flame emissivity is dominated mainly by soot, which has an emissivity of nearly unity [1-3]. Therefore, a flame with more soot will have a higher emissivity than a flame which produces less soot. This relationship is also true inside the combustion chamber of the optical engine; an operating

6

condition that produces more soot will appear hotter (emit more energy) than one with lower particulate amounts at the same temperature. Concentrations of different substances also play an important part in the amount of energy radiated. For example, oxygen and nitrogen emit very little energy in the range of temperatures experienced in an engine [4]. Therefore, a large local concentration of air in a given area will appear cooler than the actual temperature of this area. In particular to this application, the intensity of the edges the fuel plumes may be lowered because of the entrainment of air in this area. Likewise, in areas with high concentrations of substances with high emissivities, such as soot, higher temperatures may be estimated than those actually experienced in these areas. These facts must be considered during analysis.

1.1.2 Advantages and Insufficiencies of Infrared Techniques

It is beneficial to view the fuel spray using infrared techniques. The benefit in using this technique over techniques involving the visible range is because the fuel vapor is nearly transparent in the visible range. However, in the infrared region, the fuel spray is easily seen. This effect, coupled with the fact that the oxygen and nitrogen in the cylinder do not emit heavily in the infrared band until higher temperatures, allows for distinction of the fuel spray plumes.

Combustion energy is also beneficial to view using the infrared camera. The radiating products of combustion are easily seen in the infrared range. This is in comparison to high-speed images where these species are not necessarily seen. From the infrared images, the heat release of combustion may be seen better than in the visible range.

Infrared thermography does have shortcomings. As stated before, some hot gases, such as oxygen and nitrogen, have low emissivities and are mostly transparent in the infrared wavelengths. This means that the temperature measurement will be from radiation which is transmitted through the gas, rather than the radiation emitted by the gas. Even when gases emit energy, they may still appear translucent in the infrared range, especially in areas where concentrations are low. This causes difficulties in determination of temperatures in these areas.

Another major disadvantage of current infrared technology is the speed at which data acquisition can be made. In this application, infrared cameras are limited to one usable frame per cycle. The visible high-speed camera used is able to capture many more pictures per cycle. Because of the lower speed of the infrared camera, cycle-to-cycle variations will appear in these pictures.

1.2 High-speed Imaging Techniques

The advantages of using high-speed visible imaging techniques lie in the ability to acquire many more usable pictures per cycle compared to infrared imaging techniques. The high-speed camera used for these experiments is coupled with a copper vapor laser. The laser allows for the illumination of fuel injection events when there would otherwise be too little light. This method relies on the scattering of light by fuel droplets. Thus, as the droplets evaporate the fuel becomes increasingly difficult to view. The camera is also able to capture visible light radiation emitted from combustion reactions. The main advantage of this technique is that information within individual engine cycles can be deduced because of the higher acquisition frame rate.

1.3 In-cylinder Pressure

In-cylinder pressure signals are also very important in the analysis of combustion events within an engine cycle. The pressure analyses presented here include indicated mean effective pressure (IMEP), mass fraction burned (MFB), and heat release rate (HRR). Trends can be correlated with the acquired images. Evaluation of these parameters can be applied in conjunction with the infrared techniques to gain more insight into the events. The results of individual cycles are used to determine the differences in performance from one cycle to the next.

1.4 Previous Work

Some work has been done with optical Diesel engines using either visible or infrared imaging. The difference with other work and the work presented in this paper is the production of images of both imaging techniques simultaneously. There were no published papers found with this technique used. The papers discussed in this section provide good background for the discussions developed later.

A useful study on this subject is the 1999 SAE paper by Anders Larsson titled "Optical Studies in a DI Diesel engine" [1]. In these experiments, Larsson uses an endoscope and the two color method to determine soot amounts and temperature inside an in-cylinder Diesel flame. It is presented that, for a flame in the visible wavelengths, soot is the largest optical radiator. It is also presented that the flame temperatures range from 1800 K to 3000 K.

Another useful study using an optical engine is the paper by Tominaga et al. [5] titled "Flame Temperature Measurement in Diesel Engine on Two Color Method utilizing CMOS Camera". The experiments in this paper were completed with an optical engine with a piston window. This paper presents maximum flame temperatures up to 2400 K using a two color method with a CMOS camera. This result is in agreement with the paper published from the DEER 2003 conference by Pickett and Siebers [6] which states Diesel flame temperatures can exceed 2600 K.

Other flame temperature studies have been completed. In the papers by Brahmi et al. [7], Brisely et al. [8], and Konishi et al. [9] flame temperatures are found using different optical techniques. In these papers, flame temperature ranges are presented from 1000-2000 K. The paper by Brahmi et al. is of particular interest in their estimation of flame emissivity values in the range of .4-.7.

Another useful paper to the infrared imaging work is the paper titled "Infrared Spectral Analysis of Engine Preflame Emission" by Marcis Jansons et al. [2]. In this work, a spark ignited single cylinder optical engine was used with infrared cameras. An infrared camera and a sprectrometer were used to gather data through a piston window in a Bowditch piston. This paper also develops a model for emissivity values and presents an emissivity range of 0.55 to 0.9. Emissivities of flames and infrared techniques are also discussed in a paper by Planas-Cuchi et al. titled "Determination of Flame Emissivity in Hydrocarbon Pool Fires Using Infrared Thermography" [3]. In this paper, values of emissivities of flames are seen to be between 0.7 and 0.95 for hydrocarbon diffusion flames.

The soot concentration of flames is shown as a main cause of the differences in emissivity. It is therefore necessary to understand the particulate production within engines. The book Particulate Emissions from Vehicles by Peter Eastwood [10] and the 2002 SAE paper "Optical Investigation of the Effect of Fuel Jet Wall Impact Position on Soot Emissions in a Single Cylinder Common Rail Direct Injection Diesel Engine" [11] are both excellent references on this subject. It is presented that wall impingement of the fuel spray has a direct impact on the amount of soot produced. Fuel droplet size and engine load are also shown to have an effect on particulate production, as presented in the papers by Xu et al. [12] and El-Shobosky [13] respectively. With soot production better understood, it is necessary to better understand its effect on flames. The paper by Huang and Zhang [14] and the 2000 SAE paper by Fettes et al. [15] discuss the effects of soot inside flames. These papers show the coloration of flames depending on soot amount. It is shown in the visible range that the flame is skewed towards a red color by an increase in soot.

Through the previous work reviewed here, a better understanding of the principles involved in this project is created. Some work has been done gathering images using a single imaging setup, but none was found to use the simultaneous techniques used in this project. In-cylinder temperatures of up to 3000 K can be expected. Emissivity values range from .4 to .95, depending on soot production. This information will be extremely useful in the later stages of this paper's discussion.

CHAPTER 2

EXPERIMENTAL SETUP AND PROCEDURE

The data acquisition in this project was accomplished using an optically accessible Diesel engine, a high-speed camera, an infrared camera, and pressure acquisition equipment. The optical Diesel engine is a single cylinder engine based on a production engine. Many parts of the engine system are custom fabricated. The high-speed camera used is able to acquire images over individual cycles whereas the infrared camera is only able to take a single usable picture for each event. These cameras are used in conjunction with each other to simultaneously take the same event. Pressure data are able to be stored using a data acquisition system. A fuel collection system was used to measure the amount of fuel per injection of the nozzles for different pulse widths. The use of this hardware gives abilities that are well suited to this project.

2.1 Engine

An optically accessible Diesel engine was used in these experiments. The engine used was a single cylinder optical engine based from a 4.5 L V6 International VT 275 Diesel engine. This engine was designed to use as much hardware as possible from the production engine. The slider-crank kinematics were taken into account during the design process and are nearly identical to the original engine configuration. The bore and stroke are 95 mm and 105mm respectively. The engine has approximately an 18:1 compression ratio. The production connecting rod is used. A Bowditch style piston with a sapphire piston insert is used for optical access. This piston is an extension of the production

piston and is used such that a mirror can be placed under the window in the piston in order to view the combustion chamber. A view of the piston can be seen in Figure 1. Optical access was available through the bore centerline and into the combustion chamber by use of a gold first surface mirror and through the sapphire piston insert. Graphite piston rings are used to seal the combustion chamber. The engine was fitted with a pressure transducer placed in lieu of a glow plug to achieve in-cylinder pressure data. The engine head and cylinder are preheated using a temperature controlled hot water system. The intake system of the engine is connected to compressed air and nitrogen cylinders via a set of lines and valves, allowing for variation of oxygen content and boost of the incoming gas mixture. An ECM AFRecorder was used to measure oxygen content. Figures 1 and 2 are views of the engine setup. The injection system used was a common rail pressure system modified for this particular application. Two piezo injectors were used; a different injector was used with each nozzle. The nozzles used were a 6-hole and a 7+7-hole nozzle. The six-hole nozzle has holes of 0.185 mm with injection angles of 154 degrees. The 7+7-hole nozzle has 14, 0.075 mm holes evenly spaced around its circumference with alternating cone angles of 170 and 150 degrees. The injector used with the 6-hole nozzle was expected, from previous experience, to be more consistent, as this design is closer to a production design.
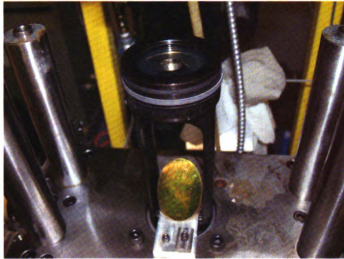
Figure 1: View of the Bowditch piston and gold mirror used to reflect along the centerline of the bore.
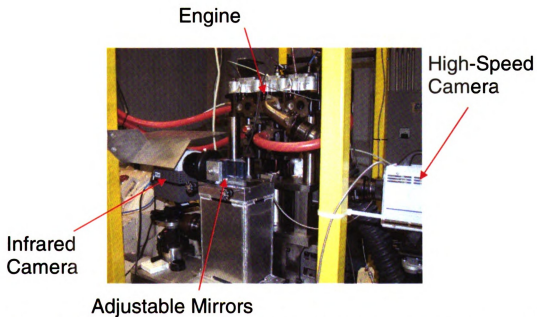
Figure 2: Experimental setup for the optical single cylinder Diesel engine showing camera positions relative to the engine.
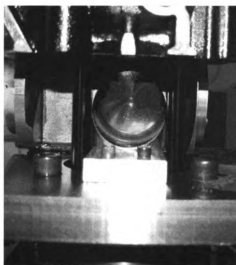
Figure 3: View of the gold first-surface mirror allowing for views along the centerline of the engine cylinder.

2.1.1 Operating Conditions

The goal of these experiments was to gain insight into the fuel spray and combustion characteristics of the different nozzles. Data were gathered at different operating conditions in order to accomplish this. The operating conditions for these experiments are found in Table 1. All experiments were performed at 1500 rpm, an intake pressure of 1.5 atm, and a coolant temperature of 190°F. For all cases, an injection timing of 12 crank angle degrees (CAD) before top dead center (BTDC) was used.

Table 1: Operating conditions.

Nozzle	Injection Pulse Width (ms)	Fuel Injected (mg/injection)	Inlet Oxygen Content (%Oxygen)	Fuel Rail Pressure (bar)	Purpose
6-Hole	0.63	46.25	13.3	2000	Combustion
6-Hole	0.55	35.25	13.3	2000	Combustion
6-Hole	0.55	35.25	0	2000	Fuel Spray
7+7-Hole	1	46.25	13.3	2000	Combustion
7+7-Hole	0.82	35.25	13.3	2000	Combustion
7+7-Hole	0.82	35.25	0	2000	Fuel Spray

2.1.2 Engine Data Acquisition Procedure

The general procedure for engine operation is as follows:

- The engine was disassembled by pulling the cylinder and head assembly upwards, above the piston. The piston window was then thoroughly cleaned. All other optics were also cleaned, if needed.

- The engine was reassembled.

- The engine head and cylinder assembly was heated to 190°F.

- The engine was motored up to operating speeds. The timing of the engine encoder was checked. Oxygen content was set to the desired operating point. Fuel rail pressure was set. The data acquisition system was set to begin recording. The laser block was removed.

- The injector was activated, thereby triggering the cameras as well.

- Once the needed amount of cycles was completed, the injector was stopped, the laser block replaced, and the engine motored down.

2.2 Cameras

2.2.1 Infrared Camera

The infrared camera used was a FLIR Phoenix MID infrared camera. This camera has a viewable wavelength region from 3-5 μm. This is a liquid cooled camera with the ability to be triggered by a 5V transistor-transistor logic (TTL) pulse. The acquisition speed of this camera is limited to 60 frames per second (fps), meaning, at 1500 rpm, one

picture can be taken every 57.6 CAD, thereby allowing for only one usable picture per combustion or fuel spray event.

2.2.2 High-Speed Camera

The high-speed camera used is a Photron Fastcam APX RS, which has the ability to acquire images in the visible light wavelength range at 10,000 fps with a 512 x 512 pixel resolution. This speed translates to the ability to capture one picture every 0.9 CAD, thereby allowing many more pictures per event than the infrared camera can acquire. Like the infrared camera, the high-speed camera also has the ability to be triggered with a 5V TTL pulse. This camera is coupled with a copper-vapor laser directed along the centerline of the bore for illumination of the engine cylinder in order to view the fuel spray with this camera. The laser creates a beam centered at approximately 550 nm, causing the green hues seen in the high-speed pictures presented later. The width of the laser pulse is 25 ns. The laser frequency is driven by the high-speed camera output at 10,000 pulses per second.

2.2.3 Camera Setup

The cameras are placed opposite each other and reflect off gold mirrors placed between them such that both cameras can view the cylinder at the same time, as seen in Figures 4 and 5. This setup allows for the acquisition of an entire cycle by the high-speed camera with one corresponding picture per cycle from the infrared camera for that cycle. The drawback to this setup is that the lines of sight of the different cameras lead to slightly different pictures. That is, there is some skewing along the centerline of the

17

cylinder due to the different angles of the cameras required to achieve this setup. The mirrors skew the view of the mirror at the bottom of the engine cylinder such that some optical access is lost from this mirror. This causes the dark regions on the edges of the pictures as seen in Figure 6. It is important to note that some attenuation of the pictures also occurs due to the experimental setup. In order to illuminate the engine cylinder it was necessary to use a copper vapor laser beam transmitted through a fiber optic cable. The casing to the cable causes some interference and is the shadow seen at the bottom and left side of the images. Figure 6 and Figure 7 show the effect of skewing and interference with hardware. These pictures have the highlighted areas of interference and attenuation due to the experimental setup highlighted in red. These effects must be noted for subsequent results presentations.
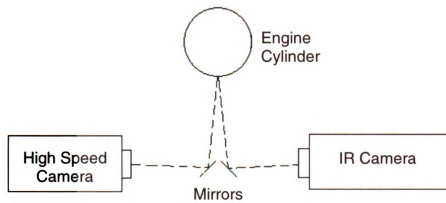
Top View

Figure 4: Top view diagram of the camera setup relative to the engine.
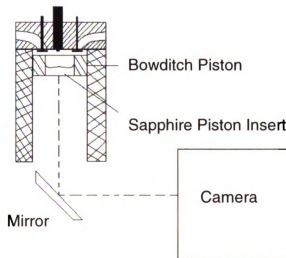
Side View

Figure 5: Side view diagram of the camera setup relative to the engine.

Figure 6: Infrared picture with the edge that is attenuated due to mirror setup highlighted in red.
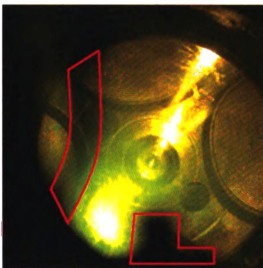
Figure 7: High-speed picture with the areas of hardware interference causing shadows in the picture highlighted in red.
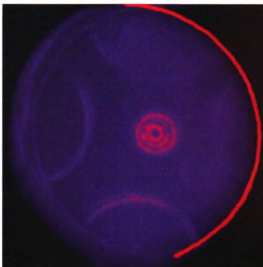
2.2.4 Infrared Camera Settings

Two settings were used for the infrared camera: one for the in-cylinder fuel spray experiments and one for the in-cylinder combustion experiments. The settings were similar in that an integration time of 0.02 ms was used along with the same 100 mm lens for each experiment. A neutral density filter allowing 3.5% of energy through for the camera viewing wavelengths was used for the in-cylinder combustion experiments. This filter was not used for the in-cylinder fuel spray experiments. The neutral density filter was used to restrict the energy seen by the camera such that the images would not be overexposed.

2.2.5 High-Speed Camera Settings

The high-speed camera maintained the same settings for all experiments. A shutter speed of 98 µs was used with a frame rate of 10,000 fps. When coupled with the laser, the camera settings allowed for illumination of the fuel spray while also allowing for viewing of combustion with the high-speed camera.

2.2.6 Camera Triggering

For image acquisition, forty-one consecutive cycles were used. A computer program was used to trigger the infrared camera at a set of delays in 100 µs increments, starting with a zero delay and adding 100 µs for each subsequent cycle. The high-speed camera ran at 10,000 fps for 100 frames, triggered using the injection pulse and thereby capturing the entire fuel spray or combustion event. This acquisition setup would then give 41 frames taken at the same timing in the infrared and visible ranges at progressing

21

delay steps while also maintaining individual cycle data with the high-speed camera. That is, each high-speed picture is paired with an infrared picture, then another pair from the next consecutive cycle and delay step, and so forth. A composite cycle can then be created from the corresponding frames of the infrared and high-speed cameras. The composite cycle will be of a picture every 0.9 CAD from different cycles, beginning with the injector activation pulse at 12 CAD BTDC and lasting until the end of combustion found from the pressure data at 24 CAD ATDC. The composite cycles produced by this technique will contain the differences caused by the cycle-to-cycle variations inherent to internal combustion engines. Using this technique, composite cycles from paired images can be produced as well as maintaining individual cycle data within the high-speed frames.

2.3 Temperature Calibration

2.3.1 Flame Box

A flame box was used to isolate a flame and safely vent the products of combustion when creating the temperature calibration files for the infrared camera. The flame box is simply an aluminum box that restricts interference from outside radiation when calibrating the infrared camera for temperature. There is a vent at the top of the box that allows for safe exhausting of the combustion gases. The walls inside the box are painted matte black such that there will be no radiation reflected, giving a constant temperature blackbody behind the flame and thereby reducing calibration errors. There is a slit cut in one wall, which allows for the placement of a torch and thermocouple. On the wall perpendicular to this wall, there is a hole cut such that the camera may be placed and

the flame viewed. One wall is a door that can be opened in order to place different objects in the camera's view, such as a gold mirror and a sapphire piston insert. A breadboard is attached to the bottom of the box for rigid mounting of these objects. Figure 8 is a view of the outside of the flame box showing the vent, door, thermocouple, and torch. Figure 9 shows the thermocouple, torch, breadboard, and hole for the camera. The flame box makes it possible to take temperature measurements of a flame using a thermocouple, to estimate an emissivity for this flame, and to create a calibration file in order to estimate temperatures inside the combustion chamber.

Figure 8: View of the outside of the flame box showing the vent, door, thermocouple, and torch.
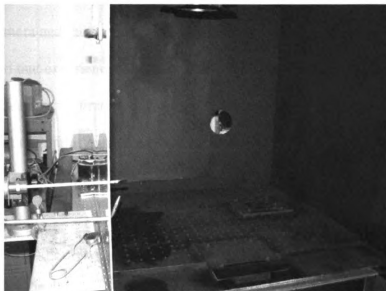
Figure 9: View of the inside of the flame box, showing the thermocouple, torch, breadboard, and camera hole.

2.3.2 Temperature Calibration Procedure

In order to calibrate the infrared camera to estimate temperature, a flame was used in conjunction with a thermocouple. A correction file was created by reading the average radiation intensity at the underside of the thermocouple in the flame and setting this value equal to the temperature reading of the thermocouple. This setup was used to adjust for flame emissivity. It was assumed that the emissivity inside the engine cylinder will be approximately the same as the emissivity of a propane diffusion flame burning in ambient conditions. This was found to be a good assumption, as the emissivity of the propane flame was found to have a value of approximately 0.5, as seen in Figure 10. This emissivity value is at the lower end of emissivities presented in literature which shows emissivities varying from 0.4 to 0.95 [2-3,7], but compares well for flames with lower amounts of soot. A piece of sapphire of uniform thickness was used in this calibration to

24

account for the transmissivity effects of the piston window. The sapphire was placed

between the camera and the flame in order to lower the irradiance captured by the camera

to correspond to that experienced in the engine. This calibration method is far from exact,

as local concentrations of air and soot will cause errors in this calibration due to

emissivity variations and it must, therefore, be remembered that the temperature

measurements presented here are estimations.
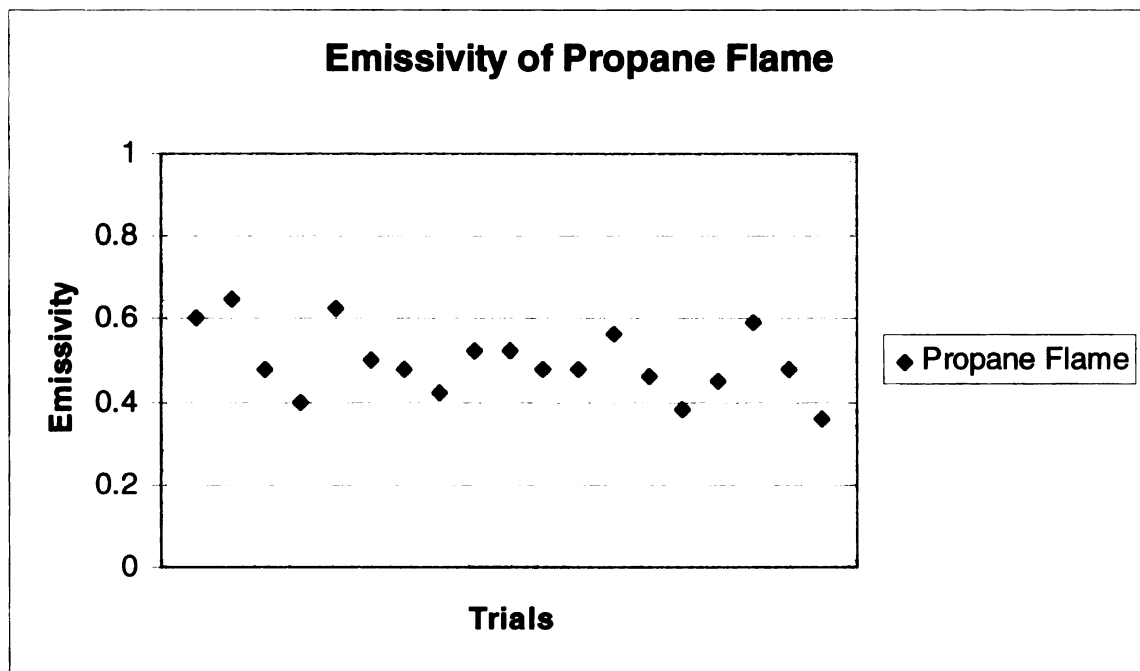
Figure 10: Emissivity values for the propane flame used in temperature calibration.

2.3.3 Infrared Scaling

The infrared pictures shown in these results are presented in color scales. This

scaling is done for visualization purposes. The images are presented in an "Ironbow"

scale. This scale presents the highest intensities as yellow-whites. Going down the

intensity scale, orange is next, followed by red, violet, blue and finally black at the lowest

end of the intensity scale. This scale allows efficient visualization of temperature gradients. The conversion effects are made evident in Figure 11. This figure is a view of the same picture with a color scale applied to show the temperature gradients. The scales used between the experiments are different. However, within the same experiment, the scales are the same. That is, the in-cylinder fuel spray images are shown in one same scale and the in-cylinder combustion images are shown in a different scale. The temperature scale of the in-cylinder combustion images can be seen in Figure 12 at the right edge of this combustion image. The temperature scale of the in-cylinder fuel spray experiments was not estimated.
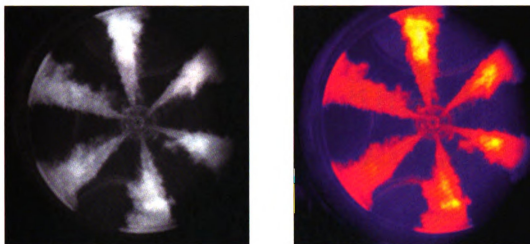
Figure 11: A Fuel spray image visualized with aid of color scales.
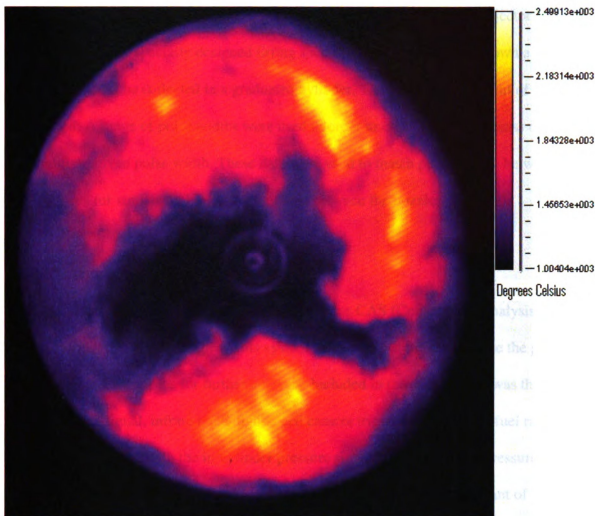
Figure 12: A combustion image including the temperature scale in degrees Celsius used in the combustion images.

2.4 Fuel Mass Injection

The mass of fuel injected per injection is needed in order to relate the amount of fuel injected with regards to the pulse width and the nozzle type being used. This experiment was done such that, for different injector nozzles, the same amount of fuel would be injected in order to match operating conditions. The fuel injector was pressurized to 2000 bar using the common rail fuel system and was injected into

atmospheric pressure. Fuel collection was accomplished by activating the injector outside

of the engine into a specially designed fitting such that the fuel would run down a length

of line and would be collected in a graduated cylinder. The volume and weight of fuel

were noted. A range of pulse widths were used in order to create a curve of mass of fuel

injected for a given pulse width. These data were used to match pulse widths between the

two injectors for similar fuel injection amounts between the nozzles.

2.5 Data Acquisition System

The data acquisition system used is a Baseline CAS (Combustion Analysis

System) from AND Technologies. This system was used to store and analyze the pressure

data as well as export files for further analysis. Included in the data storage was the

injection pulse signal, infrared and high-speed camera trigger pulse signals, fuel rail

pressure value, along with the in-cylinder pressure signal. The in-cylinder pressure

transducer used was a Kistler piezoelectric pressure transducer with a constant of 19.1

pC/bar. Data were recorded at intervals of 1 CAD resolution. This system also gives real

time feedback of in-cylinder pressures for more precise engine operation.

CHAPTER 3

RESULTS AND DISCUSSION

Images of combustion and fuel spray in the infrared and visible ranges have been acquired for two nozzles, each at two load conditions. In-cylinder fuel spray experiments were conducted to visualize the fuel mixing capabilities of the different nozzles. Experiments were conducted utilizing in-cylinder combustion to gain a better understanding of the performance of the different nozzles. It is seen that infrared imaging lends itself to visualizing fuel sprays and heat release better than high-speed images.

3.1 In-cylinder Fuel Spray

The in-cylinder fuel spray experiments were carried out in order to determine the ability of the different injectors to effectively distribute fuel throughout the combustion chamber. These experiments were performed using the same methodology as those with in-cylinder combustion except that the fuel was injected into nitrogen instead of air. Figure 13 demonstrates the differences of infrared versus high-speed views of the fuel spray. This figure is a view of the same event using the two different cameras. From the comparison of the images found here it is clear that the infrared images display more information, especially of the fuel vapors. For this reason, the images of this section are presented only as the infrared images for the composite cycle. The results of this section will focus qualitatively on the fuel distribution of the injectors.
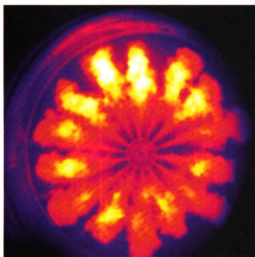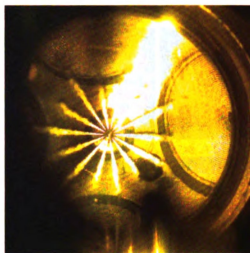
| Infrared | High-speed |

Figure 13: View of the same event during fuel injection at 3 CAD BTDC from infrared and high-speed cameras; an example of the benefits of viewing fuel spray with the infrared camera.

The fuel spray images are presented as a composite cycle in Figure 11. These pictures show major differences in fuel delivery between the injectors. In this figure, infrared pictures are presented every 4.5 CAD, starting with the injection pulse at 12 CAD BTDC. All of the pictures produced from this experiment are contained in Appendices A and B. The fuel mixing characteristics and the fuel spray velocities of the nozzles are seen to be different, in large part because of the nozzle geometries. These characteristics contribute to the differences in performance of the nozzles and are discussed in more depth in this section.
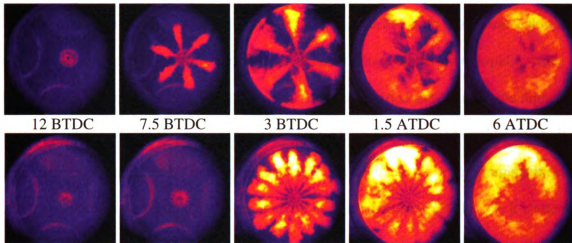
Figure 14: Infrared pictures of fuel spray for the different nozzles.

3.1.1 Fuel Mixing

The fuel mixing characteristics are important in the performance of these nozzles. The characteristics are caused by several factors, mainly nozzle design and, hence, spray velocities. The nozzle design is the most obvious cause of differences between the fuel sprays. The 7+7-hole nozzle uses two angles of smaller holes for fuel distribution at different angles, whereas the 6-hole nozzle uses one row of larger holes. The 6-hole design yields less restriction to the fuel flow because of the larger holes, thereby allowing a higher spray velocity. The increased spray velocity permits fuel to penetrate further into the combustion chamber, and, therefore, reaches more distant parts of the combustion chamber more quickly.

The spray velocities play an important part in determining how fast and to what extent the fuel mixes. The velocity can be estimated as the difference in average lengths of the fuel plumes between time steps divided by the delay step between pictures. From

the infrared pictures captured in this experiment, it is calculated that the initial fuel velocity of the 6-hole spray is approximately 150 m/s. The 7+7-hole nozzle has a slower velocity, about 75 m/s. Faster fuel sprays will penetrate the cylinder more rapidly, will tend to mix more readily, and will also tend to decrease ignition delay due to the higher relative speeds between the air and fuel spray [16]. However, increased spray velocity is not necessarily a good thing, as a higher velocity can also mean more wall impingement of the fuel spray, which could cause an increase in soot production [10-11,16]. It is seen from these images that the 6-hole nozzle has a higher spray velocity and contacts the piston bowl for a longer period of time than the 7+7-hole. This could mean a larger soot concentration found during combustion in the areas of spray impingement.

Another difference in the fuel distribution is the deflection off of the combustion bowl. The 6-hole nozzle reaches the edge of the combustion bowl around 5.7 CAD BTDC, which is much earlier than the 7+7-hole nozzle. At 3.0 CAD BTDC, when the 7+7-hole nozzle spray does reach the edge of the combustion bowl, the 6-hole spray is already being deflected by the bowl walls. The 7+7-hole nozzle distributes the fuel plumes more evenly throughout the cylinder. These plumes contact the combustion bowl, though the 6-hole nozzle plumes contact it earlier in the cycle. The plumes of the 7+7-hole nozzle are less dependent on deflection by the combustion bowl and more dependent on nozzle geometry to distribute and mix the fuel. The clockwise swirl in the engine cylinder is also seen in these images by the trailing vapor edges in these pictures. This effect is more evident in the 6-hole nozzle pictures, where the swirl is seen to move fuel vapors around the combustion chamber after the fuel spray is deflected by the combustion bowl.

There are certain obvious differences in the fuel distribution at the timing of the start of combustion. The SOC is found from the combustion experiments to be around 3 CAD BTDC for the 6-hole nozzle and slightly after TDC for the 7+7-hole nozzle. From the images at these timings, it is clear that the 7+7-hole nozzle distributes fuel to more of the combustion chamber than the 6-hole nozzle at their respective SOC timings. If combustion was present, it would then spread and become well developed by 6 CAD ATDC. At this point, the fuel is seen to be more evenly distributed throughout the piston bowl by the 7+7-hole nozzle, showing that this nozzle may mix the fuel with the air in the cylinder more effectively. Even though the spray velocity of the 6-hole nozzle is higher, the two rows of the 7+7-hole nozzle seem to distribute fuel throughout the cylinder more evenly due to the design of this nozzle.

3.2 In-cylinder Combustion

Experiments with in-cylinder combustion were completed and images were acquired using both the infrared and high-speed cameras. Pressure traces were recorded for each cycle. Most of the results presented in this section will focus on qualitative parameters. Qualitatively, the process of combustion can be seen and compared between the infrared and high-speed pictures. However, some parameters can be quantified. Start of combustion and its position in the cylinder can be determined from the infrared pictures. In-cylinder temperatures can also be estimated from the infrared pictures. Pressure data were also used to quantitatively analyze the performance of the nozzles.

The images gathered from these experiments can be organized according to several trends. Infrared and high-speed imaging techniques can be compared. It is also

presented that relative soot amounts can be estimated from the high-speed photographs. This adds a degree of qualitative analysis to the nozzle comparisons.

The images presented in this section (in Figures 15, 17, 19, and 21) are the composite cycles from these experiments. The entire composite cycles at 0.9 CAD resolution can be found in Appendices C-F. The average pressure traces corresponding to the imaging range are seen in Figures 16, 18, 20, and 21. In the pressure traces, 360 CAD corresponds to TDC at the end of compression. The range of CAD, from 12 BTDC to 24 after top dead center (ATDC), presented here is the beginning of injection until the end of combustion according to analyzed pressure data, as discussed before.

6-Hole Nozzle, 0.55ms Pulse width

Figure 15: Composite combustion cycle for 6-hole nozzle 0.55 ms pulse width case with
frames every 4.5 CAD beginning with commanded injection at 12 CAD BTDC.

Figure 15 (continued): Composite combustion cycle for 6-hole nozzle 0.55 ms pulse width case with frames every 4.5 CAD beginning with commanded injection at 12 CAD BTDC.

Figure 16: Average, maximum, and minimum pressure traces for the 6-hole 0.55 ms pulse width case.

6-Hole Nozzle, 0.63ms Pulse width
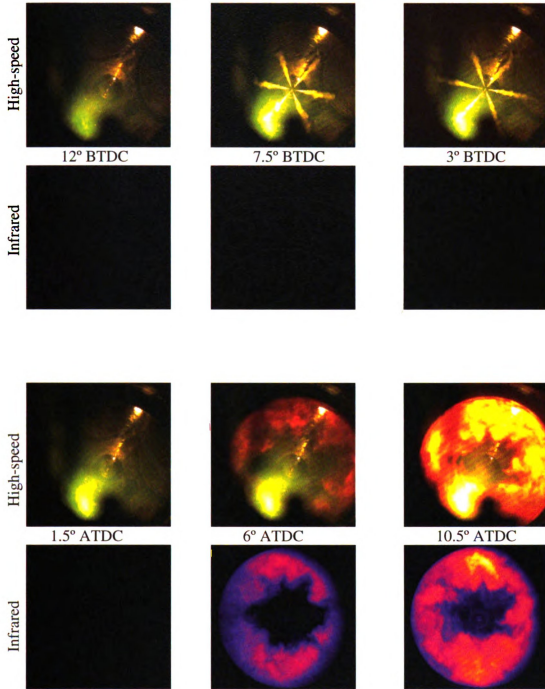
Figure 17: Composite combustion cycle for 6-hole nozzle 0.63 ms pulse width with frames every 4.5 CAD, beginning with commanded injection at 12 CAD BTDC.

Figure 17 (continued): Composite combustion cycle for 6-hole nozzle 0.63 ms pulse width with frames every 4.5 CAD, beginning with commanded injection at 12 CAD BTDC.

Figure 18: Average, maximum, and minimum pressure traces for the 6-hole 0.63 ms pulse width case.
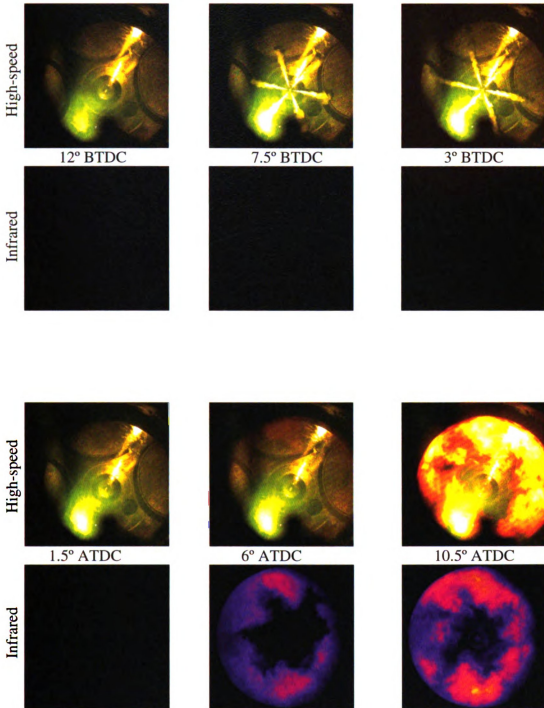
7+7 Hole Nozzle, 0.82ms Pulse Width
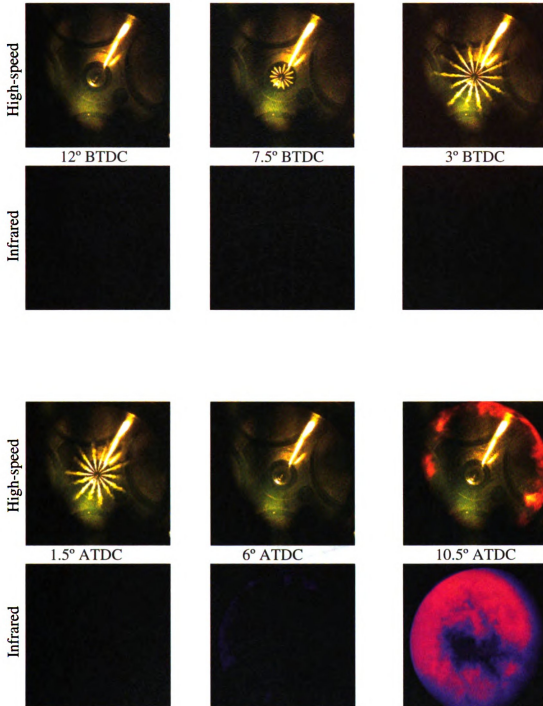
Figure 19: Composite combustion cycle for 7+7-hole nozzle 0.82 ms pulse width case with frames every 4.5 CAD, beginning with commanded injection at 12 CAD BTDC.

Figure 19 (continued): Composite combustion cycle for 7+7-hole nozzle 0.82 ms pulse width case with frames every 4.5 CAD, beginning with commanded injection at 12 CAD BTDC.
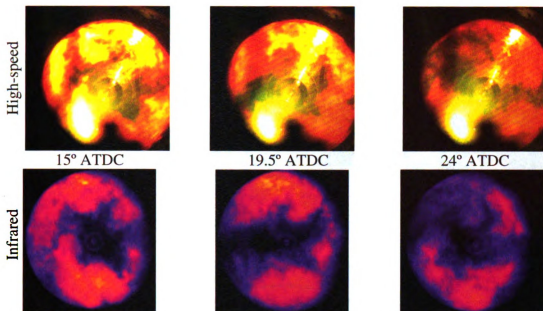

Figure 20: Average, maximum, and minimum pressure traces for the 7+7-hole 0.82 ms pulse width case.

7+7 Hole Nozzle, 1.00ms Pulse Width

Figure 21: Composite combustion cycle for 7+7-hole nozzle 1.00 ms pulse width with frames every 4.5 CAD beginning with commanded injection at 12 CAD BTDC.
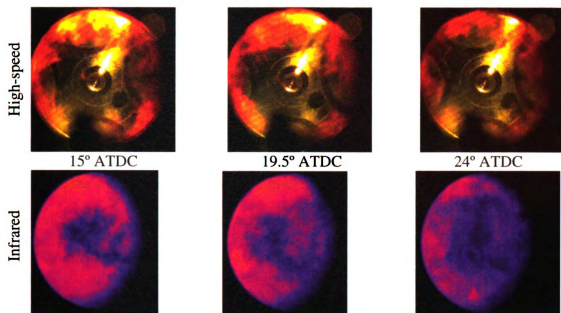
Figure 21 (continued): Composite combustion cycle for 7+7-hole nozzle 1.00 ms pulse width with frames every 4.5 CAD beginning with commanded injection at 12 CAD BTDC.
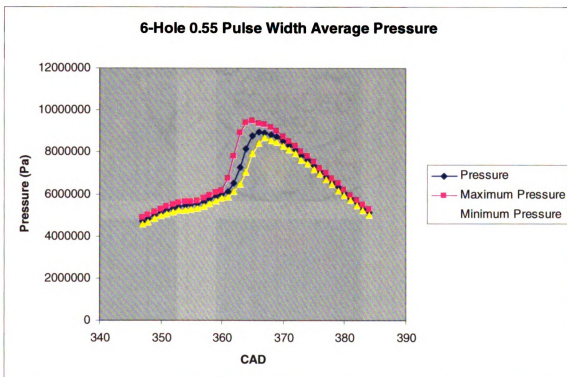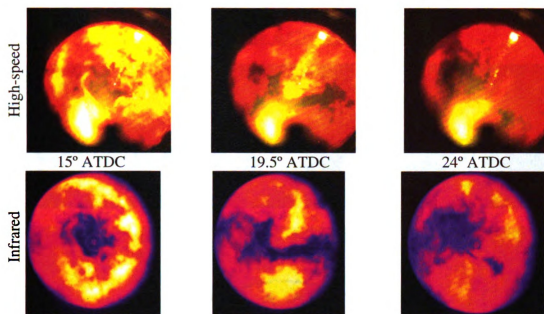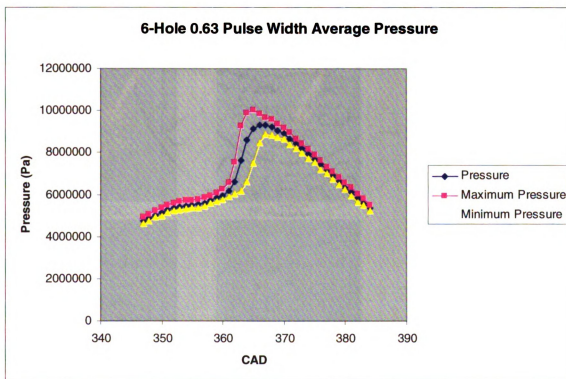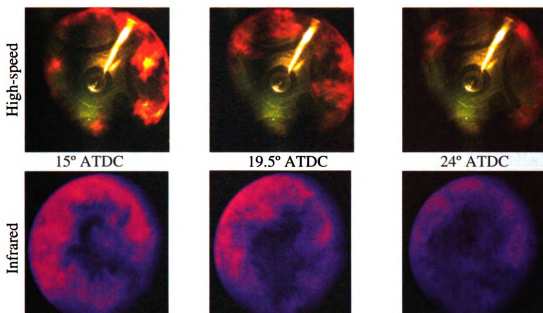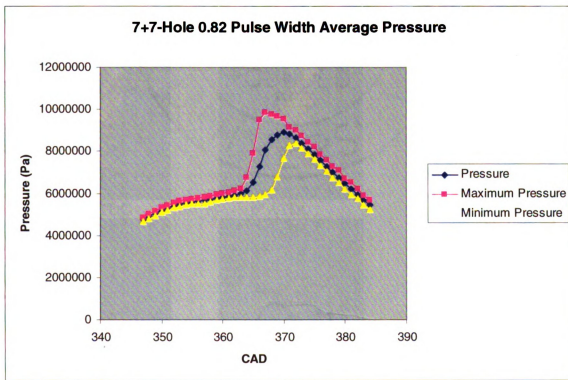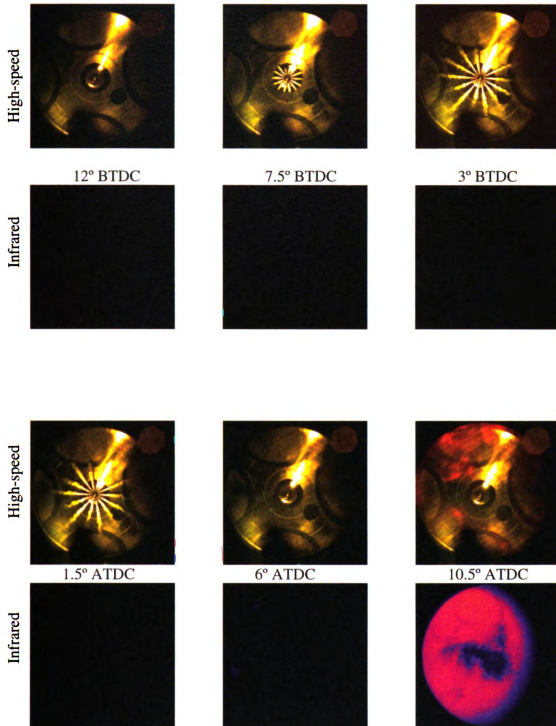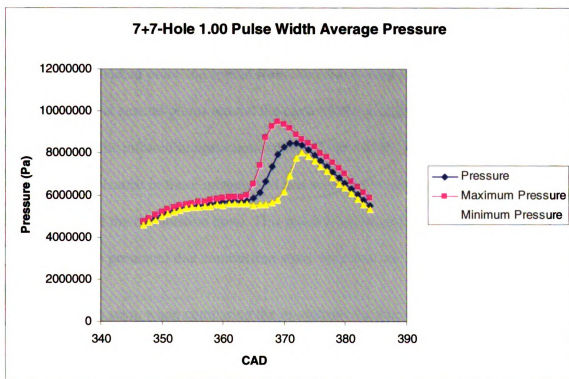

Figure 22: Average, maximum, and minimum pressure traces for the 7+7-hole 1.00 ms pulse width case.

In these images, the fuel spray is not as easily seen as in the fuel spray experiments. The high-speed frames show the fuel spray droplets, but the fuel vapors are not seen in these frames for the reasons discussed before. The high-speed images containing the fuel spray show that the behavior in these experiments is much the same as those without in-cylinder combustion, and so the location of fuel can be approximated well with the frames presented from the in-cylinder fuel spray experiment experiment. The infrared camera settings were such that the camera would view the intensity of combustion and, because of this, was unable to effectively view the vapors.

3.2.1 Start of Combustion

The start of combustion can be easily studied through these images. Once the fuel has reached the combustion bowl edge and mixed, combustion is seen in all experiments to begin at the bowl edge at numerous individual points. That is, the combustion does not start in one individual point and spread from there but is seen to start almost simultaneously at several points around the circumference of the piston bowl. This is clearly seen in the infrared images captured at 6 CAD ATDC. The initial heat release of combustion is clearest in these images, and it is seen that heat release begins at the outside edges of the combustion bowl. This result is in disagreement with previous work [17], where it is presented that combustion starts very near the injector.

It is also seen, when comparing the in-cylinder locations of the SOC to the images acquired from the in-cylinder fuel spray experiments that combustion will begin between the fuel plumes. This result is logical, as fuel evaporation will cool the area directly in and around the fuel plumes and could lead to an area of higher temperature between the

43

plumes which would serve as a local ignition source when a combustible mixture moves into this area. Combustion spreads inward and around the bowl, as seen in the subsequent images following SOC. By the end of combustion, the radiating mixture of combustion products nearly fills the entire combustion bowl in all nozzle cases, as seen in the paired images captured at 24 CAD ATDC.

3.2.2 Comparison of Different Techniques

The benefits and drawbacks of the different imaging techniques are demonstrated through these composite cycles. The 6-hole nozzle pictures show the correlation between infrared and high-speed images using the simultaneous imaging technique. Clearly, the paired pictures match up extremely well in terms of combustion energy seen at points throughout the cylinder; the infrared radiation of combustion spatially matches that captured by the high-speed camera. These pictures give confidence to the accuracy of the simultaneous technique. However, when viewing the pictures produced from the 7+7-hole nozzle, the combustion energy seen in the high-speed and infrared pictures do not match at some points in the cylinder. All of the energy released from combustion is not necessarily seen in the visible range, but is clearly evident in the infrared pictures. The infrared camera captures combustion energy throughout the most of the viewing range while the only combustion seen by the high-speed camera is a smaller amount around the edge of the piston bowl in both pulse width cases of the 7+7-hole nozzle. This result demonstrates the benefits of viewing the same event using the simultaneous camera technique. It is seen that the information gained from the infrared camera may describe combustion events and heat release more fully than the high-speed camera. However,

individual cycle analysis cannot be completed without the high-speed capabilities. The spatial differences between the two techniques warrant further analysis.

3.2.3 Soot Effects

The discrepancies in combustion energy between the infrared and high-speed images are likely caused by local differences in particulate amounts and concentrations. This is because a large amount of the visible radiation produced inside the cylinder is from soot, whereas the infrared camera is able to view all areas of heat release. That is, the radiant energy emitted by the hot gases from combustion is not necessarily captured by the high-speed camera, but is acquired by the infrared camera. Soot, on the other hand, produces a skewing of a flame to the red end of the visible spectrum, causing the orange combustion seen in the high-speed images [14]. It is, therefore, inferred that the combustion seen in the high-speed images is largely from soot radiation, as discussed in the previous work section. This inference lends itself to another possible analysis for this application: relative soot amounts can be estimated using the images acquired from the high-speed camera.

A relative soot amount can be inferred between the different nozzle cases. It has been shown that the combustion energy seen by the high-speed camera is largely produced from soot. Therefore, it is possible that the 6-hole nozzle produces more soot that the 7+7-hole nozzle, as the high-speed pictures have higher amount of visible combustion at a given CAD. This result is true in both load cases. The cause of the difference is likely because of both fuel spray impingement, as discussed before, and also on droplet size. It has been shown that smaller nozzle holes create smaller droplets,

45

thereby reducing the soot production [12,16]. It can be expected that the smaller holes of the 7+7-hole nozzle design will create smaller fuel droplets, thereby reducing soot production.

It is also seen in these pictures that the higher load cases will produce more visible combustion energy, possibly relating to an increase in the amount of soot produced for these conditions. This is in agreement with literature [13,16]. It must be remembered, however, that this view is only of the combustion bowl and does not describe the combustion events outside of the combustion bowl. An amount of soot will also form in the crevice volume here and will depend on the fuel distribution in this area [16]. It must be also considered that these conclusions are speculative and are not linked with any emissions data because of the lower available run time of this engine, for durability concerns, and the higher amount of cycles needed to gather data with available emissions equipment.

The emissivity effect of soot predicted here must be kept in mind when analyzing the temperatures estimated using the infrared camera. A higher local soot concentration will have a higher emissivity in that area. Because of these emissivity effects, the calculated temperatures may be higher than the actual temperatures inside the engine.

3.2.4 Estimated In-Cylinder Temperatures

A benefit of using infrared techniques is the ability to estimate in-cylinder temperatures. The estimation of the in-cylinder temperature field was accomplished using a correction file created and implemented by the thermography software used for infrared

data acquisition. Shortfalls, such as emissivity and concentration variations, must be accounted for, but trends can be viewed from these estimations, at the least.

In-cylinder temperatures were able to be calculated once the correction file was applied to infrared intensity data. Figure 23 shows the maximum estimated temperatures over the analyzed cycles. These data are relatively noisy due to the acquisition technique providing only one data point per delay step. However, some interesting trends are still apparent.
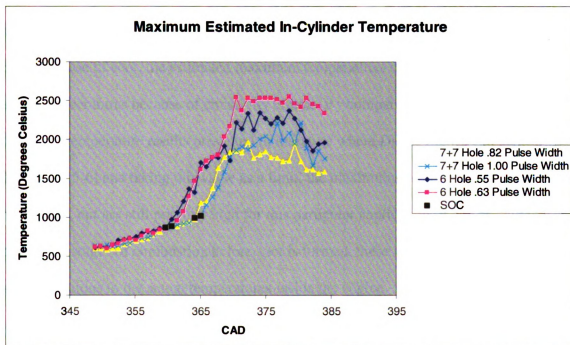

Figure 23: Maximum estimated in-cylinder temperatures for the different operating cases.

The in-cylinder temperature increase comes directly from combustion and can be correlated to the combustion events. It is seen in this plot that the 7+7-hole nozzle has a delayed SOC when compared to the 6-hole nozzle. Also, the initial increase of the 6-hole

47

nozzle curves are nearly identical while curve of the higher load of the 7+7-hole nozzle lags slightly behind that of the lower load case. As combustion slows and expansion begins, another trend is obvious: more fuel creates a higher intensity reading. This effect can be explained both with the increase in emissivity due to an increase in soot from increased fueling as well as higher temperatures from a larger energy release. Also, the longer combustion duration with the longer pulse width case of the 7+7-hole nozzle causes higher temperatures later in the cycle compared to the shorter pulse width case.

A limitation of the temperature analysis comes from the emissivity estimations used for calibration. Towards the end of combustion, when there is likely a higher concentration of soot, the estimated maximum temperatures could be higher than the actual temperatures because of emissivity effects. By comparing the presented results to the flame temperature results presented in literature where Diesel flames can approach $2500°C$ [1,5-6] and taking this value as a limit, the maximums seen here are in reasonable agreement, but are still possibly high for this particular application. It can be said that during the stages of combustion before soot is formed, these values can be very good approximations to the actual temperatures inside the engine.

Start of combustion can be seen from the plot of in-cylinder temperatures. This point is better seen in the infrared range because, in the visible range, combustion is dominated by soot radiation. The infrared camera can, however, view all the energy released as heat by the exothermic chemical reaction of combustion. The SOC point was chosen by plotting the temperature determined from the infrared pictures and choosing the point at which this curve begins to deviate from the temperature increase due to

compression. This point is seen as the black points in Figure 23. Table 2 contains the start

of combustion for the different pulse widths. From this table, it is clear that the longer

pulse width of the 7+7-hole injector causes a delay in the SOC. This is in agreement with

the pressure data analysis presented later.

Table 2: Start of combustion determined from estimated in-cylinder temperatures.

	Start of Combustion (CAD)
6 Hole .55 Pulse Width	360
6 Hole .63 Pulse Width	361
7+7 Hole .82 Pulse Width	365
7+7 Hole 1.00 pulse Width	366

The use of an infrared camera allows for analysis that is otherwise not readily

achievable. In-cylinder temperatures are estimated and the insufficiencies of the

correction methods are discussed. Start of combustion is also estimated from this

analysis. This analysis adds another dimension to the analysis presented here and

illustrates the utility of infrared applications for Diesel imaging.

3.2.5 In-Cylinder Pressure Data

The pressure data collected from the 41 consecutive cycles presented in the

previous pictures are used for further analysis. The pressure data analysis was intended as

a tool to achieve more information above that gathered from the images. Mass fraction

burned and heat release curves have been found. From these data, start of combustion can

be found, along with other trends. IMEP and peak pressure data are also presented here.

These pressure parameters give better insight into the performance of the nozzles. It is

seen that the 7+7-hole nozzle had a longer ignition delay in both load cases compared with the 6-hole injector nozzle. This is due to a combination of pulse width and air-fuel mixture properties. However, it is also seen that the 7+7-hole nozzle produced higher IMEPs than the 6-hole nozzle.

3.2.5.1 Mass Fraction Burned

Mass fraction burned (MFB) is a well defined combustion analysis parameter [18-19]. The Rassweiler-Withrow method of implementation of MFB was used in this analysis. The start of combustion is chosen as the point at which the average pressure curve begins to deviate from ideal polytropic compression when plotted in a log(P)-log(V) plot. It is shown that the mass fraction burned is the sum of the pressure rises due to combustion. The combustion pressure rises are found as the pressure rise due to a change in volume subtracted from the actual pressure rise acquired from one CAD to the next. The mass fraction burned is then defined by summing the pressure rises due to combustion until a CAD and dividing this by the sum of all of the combustion pressure rises. These curves can then be compared for the different nozzles and load conditions to analyze the differences in combustion characteristics for these systems.

The mass fraction burned curves were found from the average pressure data of the analyzed cycles. These curves allowed for determination of the average SOC along with general trends seen from the different nozzles and load cases. The mass fraction burned curves are presented in Figure 24. From these curves, SOC values were found and are presented in Table 3. The curves show several interesting trends. The 7+7-hole nozzle has a longer ignition delay, which can be expected from the lower spray velocity. The

lower velocity leads to the longer time needed to deliver and mix the fuel, as seen in the in-cylinder fuel spray experiments. It is also seen that the 6-hole curves are nearly identical, while there is some delay in the 7+7-hole nozzle for the higher load case. This is because of the lower flow rates yielding longer pulse widths, thereby shifting the curves later in the cycle. There will also be some shifting towards earlier in the cycle caused by the increase in flame speed because of the increase in equivalence ratio for the higher fueled cases [20].
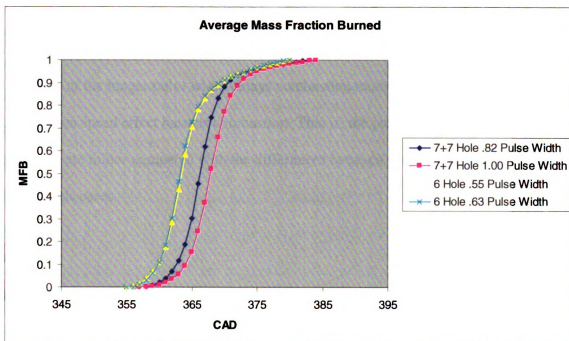

Figure 24: Mass fraction burned curves for the different nozzle operating cases from the averaged pressure traces.

Table 3: Start of combustion determined from the mass fraction burned curves.

	Start of Combustion (CAD)
6 Hole .55 Pulse Width	357
6 Hole .63 Pulse Width	357
7+7 Hole .82 Pulse Width	359
7+7 Hole 1.00 pulse Width	360

3.2.5.2 Heat Release Rate

The mass fraction burned results are echoed in the heat release rate curves. The heat release rate curves are found by calculating the first derivative of the mass fraction burned curves. These curves are presented in Figure 22. Combustion is seen to be delayed in the 7+7-hole nozzle cases, while it occurs sooner with the 6-hole. The curves from the 6-hole nozzle show that the heat release rate has a higher maximum for the higher load case, while the opposite is true with the 7+7-hole nozzle. This is likely due to the increase in combustion speed at higher load for the 6-hole nozzle, while with the 7+7-hole nozzle the effect of the longer pulse width delays combustion more significantly than the combustion speed effect hastens combustion. That is, the pulse width differences in the 6-hole case are minor compared with the differences between the pulse widths of the 7+7-hole nozzle cases.
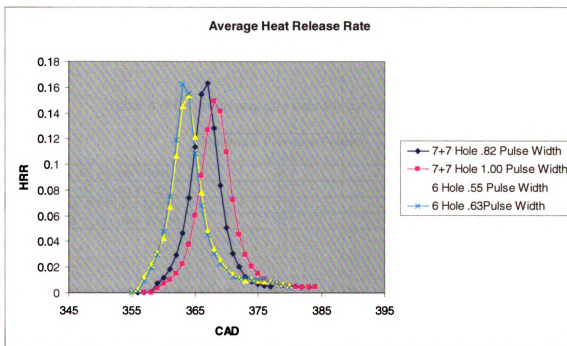
Figure 25: Average heat release rate curves found from the first derivative of the mass fraction burned curves.

3.2.5.3 Peak Pressures

Peak pressures from the optical engine used here can be compared with peak pressures from non-optical Diesel engines. Trends between the different nozzles and load cases can also be evaluated. Table 4 gives the average peak pressure and the crank angle at which this occurs for the different operating cases. These values compare well with peak pressures in non-optical Diesel engines operating at light load, which have peak pressures on the order of 90 bar, as experienced in these experiments [20]. When comparing the different operating cases, it is seen that the higher load case with the 6-hole injector leads to a higher peak pressure. However, the more delayed combustion experienced with the higher load in the 7+7-hole nozzle cases cause a slightly lower average peak pressure later in the cycle. It is also seen that the temperature estimations

agree with this pressure data, as higher peak pressures acquired with the 6-hole nozzle

correspond to higher estimated peak temperatures.

Table 4: Maximum pressure data for the cases examined.

	Maximum Pressure Position (CAD)	Average Maximum Pressure (bar)
6 Hole .55 Pulse Width	367	89.50
6 Hole .63 Pulse Width	367	93.14
7+7 Hole .82 Pulse Width	370	89.02
7+7 Hole 1.00 pulse Width	371	84.79

3.2.5.4 Indicated Mean Effective Pressures

Indicated Mean Effective Pressure is the scaled total work output from the

cylinder for the engine cycles. The IMEP for an engine cylinder is the work produced

from the compression and expansion cycles divided by the displacement of the engine

cylinder. The IMEP values presented here are the averaged pressure values calculated

from the cycles presented as before, along with the maximum and minimum values for

individual cycles. Figure 26 is a plot of the average IMEP values evaluated here. From

this plot, it is clear that the 7+7-hole injector nozzle produces higher IMEPs for a given

fuel injection amount than the 6-hole injector along with the higher overall IMEP. Table

5 shows other important data from the IMEP data. It is inferred from the data in Table 5

that the 6-hole injector produced more consistent combustion. This is likely because the

injector used for this nozzle was more consistent in fuel flow. It could also be due to the
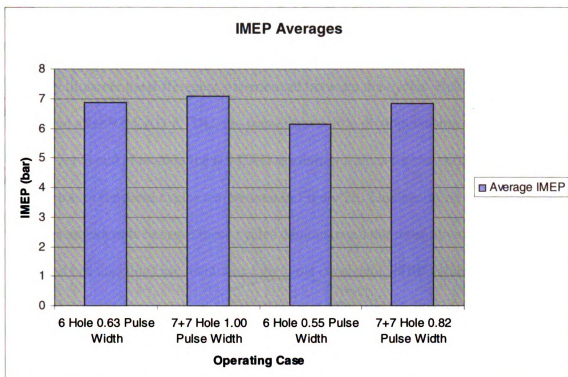
designs of the injector nozzles.

Figure 26: Indicated mean effective pressures for the different nozzles and load cases.

Table 5: IMEP data for the different operating cases examined.

	Average (bar)	Maximum (bar)	Minimum (bar)	Standard Deviation (bar)
6 Hole .55 Pulse Width	6.15	6.54	5.84	0.15
6 Hole .63 Pulse Width	6.86	7.11	6.61	0.12
7+7 Hole .82 Pulse Width	6.84	7.27	6.53	0.17
7+7 Hole 1.00 pulse Width	7.08	7.59	6.69	0.24

3.2.5.4.1 Maximum and Minimum IMEP Cycles

The average IMEP data lead to more analysis on the maximum and minimum IMEP cycles. These individual cycles can be further analyzed using the high-speed pictures and pressure traces for these particular cycles. In order to demonstrate this, the 6-hole nozzle, 0.63 ms pulse width case was chosen as an example. The frames presented in Figure 27 are from the maximum and minimum cycles of this operating condition,

beginning with the frame corresponding to 3.3 CAD ATDC and every 0.9 CAD

following, until 9.6 CAD ATDC. The pictures are organized in this way in order to

concisely illustrate the differences experienced between the cycles. Before 3.3 CAD

ATDC and after 9.6 CAD ATDC, the frames have little distinguishable differences.

Appendices G and H contain the 0.9 CAD resolution frames for the entire cycle. The

pressure traces for these cycles can be seen in Figure 28. This operating condition was

chosen as an example because these cycles demonstrated the most obvious pressure

trends and because this case maintained the most consistent IMEP values. The major

differences seen in these pictures are the timing of SOC and the intensity of the images.
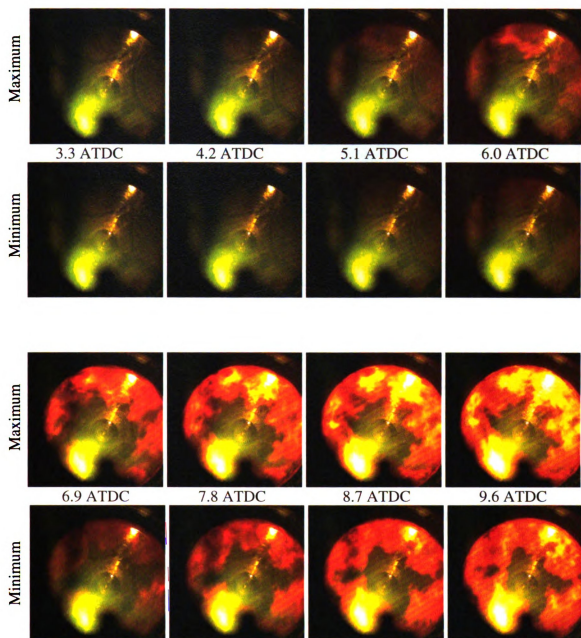
Figure 27: Frames from the max and min IMEP cycles for the 6-hole 0.63 ms pulse width case.
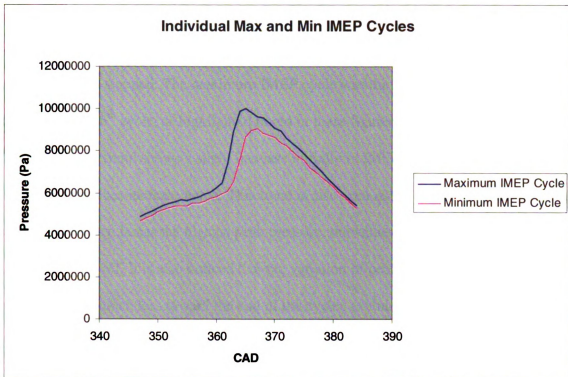
Figure 28: Pressure traces for the max and min IMEP cycles of the 6-hole 0.63 ms pulse width case.

It is seen from the data that the higher IMEP is caused by an earlier SOC and higher pressures throughout the cycle. This is seen in both the photographs and in the pressure trace. In the high-speed frames, combustion is seen earlier in the cycle for the higher IMEP cycle. The intensity of combustion is also higher throughout this cycle, as seen when comparing the combustion intensity of the frames captured at 7.8, 8.7, and 9.6 CAD ATDC. These trends are mirrored in the pressure data, where it is clear that combustion starts slightly earlier and achieves higher pressures.

Further investigation can be completed on the maximum and minimum IMEP cycles using available pressure data. It is seen that some of the differences in IMEP values are due to the transient effects of engine startup. Figures 29 and 30 demonstrate this result. Figure 29 is a plot of the IMEP values for each cycle. Figure 30 is a plot of the

peak pressures experienced for these cycles. The first cycle in these plots is the first cycle that the injector was activated. The 41st cycle corresponds to the cycle when data acquisition was stopped. The maximum IMEP cycle was the 8th cycle; the minimum cycle was the 16th cycle, as highlighted in red in these figures. It is seen in the IMEP data that the general trend shows a slight increase initially in IMEP followed by a decrease and then the values increase again. This trend is also seen in the plot of the peak pressures where the first cycle has the highest peak pressure, the values decrease and then increase again and level off. It is also noticed that the variation of peak pressures between a cycle and the next is much less toward the end of the cycles examined. A good explanation for the variability in IMEP values comes from these transient effects. The startup effects can be explained by the increase of the cylinder temperature from the heating of combustion and also from internal exhaust gas recirculation. This trend was seen in all nozzles and fueling cases and must be remembered when reviewing the pictures presented before as a possible explanation for variability in these data.
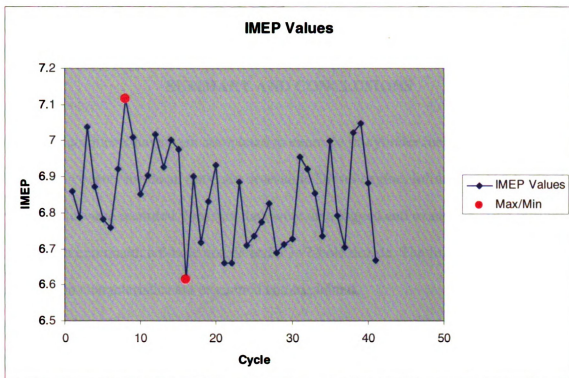
Figure 29: IMEP values plotted over the examined cycles with the maximum and minimum values highlighted with red circles.
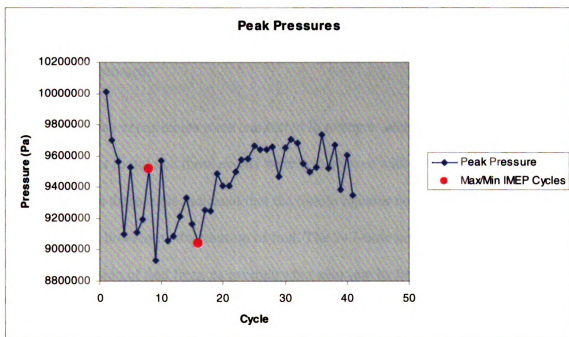

Figure 30: Peak pressures plotted over the examined cycles with the maximum and minimum IMEP cycle values highlighted with red circles.

CHAPTER 4

SUMMARY AND CONCLUSIONS

Experiments have been completed to examine in-cylinder fuel injection and combustion events inside an optically accessible Diesel engine. Infrared and high-speed photographs were recorded. Pressure data were also logged and examined. Two injector nozzles are examined; a 6-hole nozzle and a 7+7-hole nozzle. The fuel spray and combustion characteristics are examined and explained.

The experimental setup utilized for these experiments allowed for acquisition of data that are otherwise inaccessible. The engine design used in these experiments maintained parts and geometries as close to production as possible. The fuel system consists of a common rail system with a piezo injector. An infrared camera and a high-speed camera were used in conjunction with a pressure data acquisition system for data attainment and storage.

Fuel spray experiments were conducted in nitrogen such that combustion would not occur. It was found that these events were best viewed with the infrared camera. The data found from these trials indicated that the 6-hole injector nozzle was aided more by the combustion bowl in its distribution of fuel. The 7+7-hole nozzle created a more uniform dispersion of fuel from its geometry but also saw its fuel spray plumes deflected off of the combustion bowl to a lesser extent than the 6-hole fuel spray. The 6-hole nozzle penetrated deeper into the combustion bowl due to the higher spray velocities from larger nozzle holes. It is determined that the 6-hole nozzle penetrated the

combustion bowl deeper, but the 7+7-hole nozzle tended to distribute fuel more uniformly.

Combustion experiments were completed with the goal of viewing the heat release and gaining insight into the performance of the different nozzles, each under two load conditions. Comparison of the pictures and pressure data produced from these experiments showed the differences in performance between the two nozzles. Infrared photography showed a start of combustion earlier than was seen in the high-speed pictures. However, mass fraction burned curves showed start of combustion earlier than was seen by either camera. In-cylinder temperatures were estimated from the infrared pictures. The trends found from this analysis mimicked those found from pressure data. The start of combustion was seen to be lagging in the 7+7-hole nozzle cases compared with the temperature curves of the 6-hole nozzle. Predicted max temperatures of around 2500°C were likely higher than actually experienced because of the increase of local emissivities due to soot concentrations. The high-speed pictures showed a possible higher soot production for the 6-hole nozzle than 7+7-hole. The mass fraction burned curves showed a longer ignition delay and combustion duration for the 7+7-hole nozzle likely due to the longer pulse widths required for the same amount of fuel injected between different nozzles. Heat release rate curves also showed these results. Indicated mean effective pressure results showed a higher performance with the 7+7-hole nozzle for both load cases. Minimum and maximum IMEP cycles were compared for the 6-hole 0.63 ms pulse width case, demonstrating the increase in pressure and start of combustion, thereby improving performance. The SOC and energy increase trends were evident in the visible high-speed frames for these cycles. Overall, higher pressures and temperatures were

produced with the 6-hole nozzle while the 7+7-hole nozzle produced possibly lower soot amounts while yielding higher IMEP values for these operating conditions.

The main conclusion found from these experiments is the simultaneous techniques presented here can achieve data which are otherwise nearly impossible to acquire. The infrared pictures show a higher amount of information about in-cylinder fuel spray and combustion than the high-speed frames. The high-speed frames give a larger amount of individual cycle information. Pressure data allow for explanation of some of the trends seen in the images.

CHAPTER 5

RECOMMENDATIONS

1. Emissions data should be gathered with a more durable engine in order to relate this data with the soot predictions here. This could then provide credence to the soot observations. Other emissions data could also be gathered and analyzed.

2. Hardware should be modified to reduce interference in the images. A beam-splitter should be used to eliminate the attenuation caused by the mirror setup. The mounting hardware for the fiber optic cable could also be modified to eliminate some of these effects. This would allow direct correlation between the infrared and high-speed pictures, without having to adjust for the lines of sight..

3. More nozzles, load cases, and injection timings should be tested with these methods. This will better explain some of the trends seen in these analyses.

4. If possible, the same injectors should be used for both nozzles. This will eliminate some of the uncertainty between the nozzles.

5. CFD codes should be validated and used in conjunction with these results. This will give credibility to the simulations. It will also be useful to use these results to estimate emissivities and explain some trends which are not entirely understood.

APPENDICES

APPENDIX A

INFRARED IMAGES OF IN-CYLINDER FUEL SPRAY - 6-HOLE NOZZLE

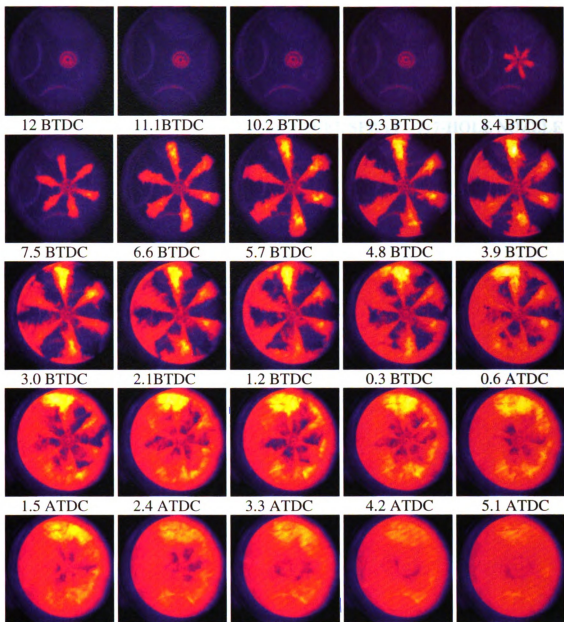| 12 BTDC | 11.1 BTDC | 10.2 BTDC | 9.3 BTDC | 8.4 BTDC |
7.5 BTDC	6.6 BTDC	5.7 BTDC	4.8 BTDC	3.9 BTDC
3.0 BTDC	2.1 BTDC	1.2 BTDC	0.3 BTDC	0.6 ATDC
1.5 ATDC	2.4 ATDC	3.3 ATDC	4.2 ATDC	5.1 ATDC

Figure 31: In-cylinder fuel spray images from consecutive cycles for the 6-hole nozzle.

APPENDIX B

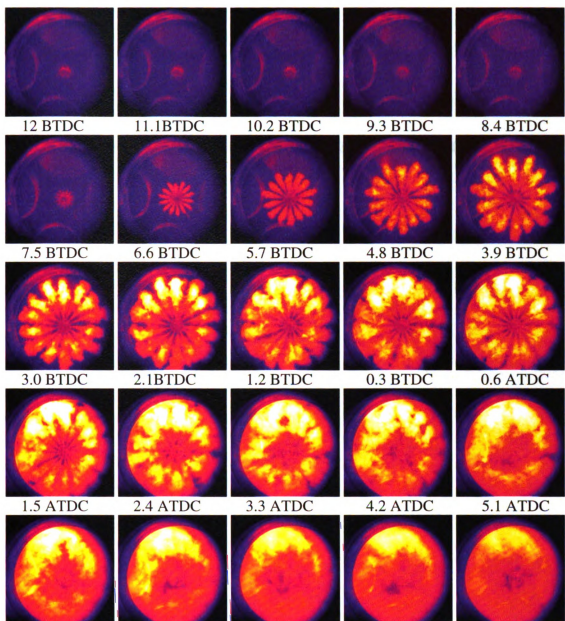## INFRARED IMAGES OF IN-CYLINDER FUEL SPRAY - 7+7-HOLE NOZZLE

12 BTDC	11.1BTDC	10.2 BTDC	9.3 BTDC	8.4 BTDC
7.5 BTDC	6.6 BTDC	5.7 BTDC	4.8 BTDC	3.9 BTDC
3.0 BTDC	2.1BTDC	1.2 BTDC	0.3 BTDC	0.6 ATDC
1.5 ATDC	2.4 ATDC	3.3 ATDC	4.2 ATDC	5.1 ATDC

Figure 32: In-cylinder fuel spray images from consecutive cycles for the 14-hole nozzle.

APPENDIX C
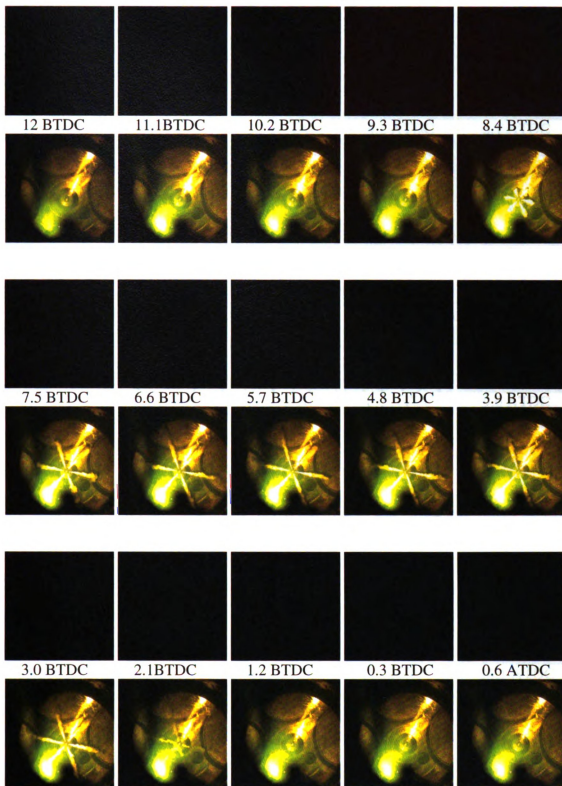

COMPOSITE CYCLE OF 6-HOLE NOZZLE, 0.55 PULSE WIDTH

Figure 33: Composite engine cycle at 0.9 CAD increments for 6-hole nozzle, 0.55ms pulse width case. The infrared images are above the CAD, high-speed images are below.
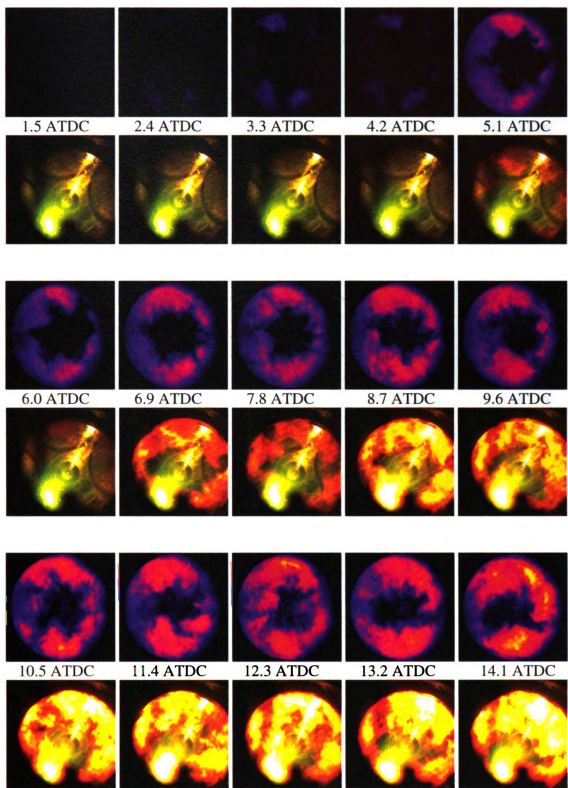
| 1.5 ATDC | 2.4 ATDC | 3.3 ATDC | 4.2 ATDC | 5.1 ATDC |

| 6.0 ATDC | 6.9 ATDC | 7.8 ATDC | 8.7 ATDC | 9.6 ATDC |

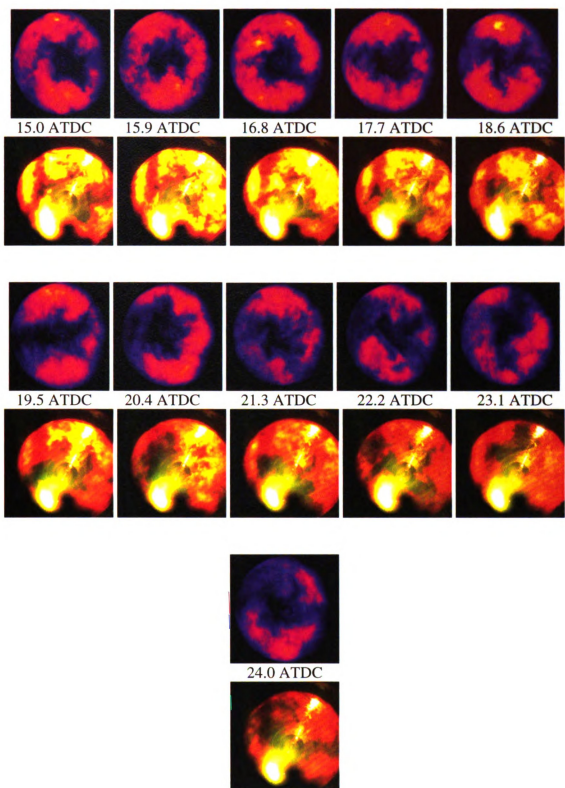| 10.5 ATDC | 11.4 ATDC | 12.3 ATDC | 13.2 ATDC | 14.1 ATDC |

Figure 33 (continued): Composite engine cycle at 0.9 CAD increments for 6-hole nozzle, 0.55ms pulse width case. The infrared images are above the CAD, high-speed images are below.

| 15.0 ATDC | 15.9 ATDC | 16.8 ATDC | 17.7 ATDC | 18.6 ATDC |

| 19.5 ATDC | 20.4 ATDC | 21.3 ATDC | 22.2 ATDC | 23.1 ATDC |

24.0 ATDC

Figure 33 (continued): Composite engine cycle at 0.9 CAD increments for 6-hole nozzle, 0.55ms pulse width case. The infrared images are above the CAD, high-speed images are below.

APPENDIX D

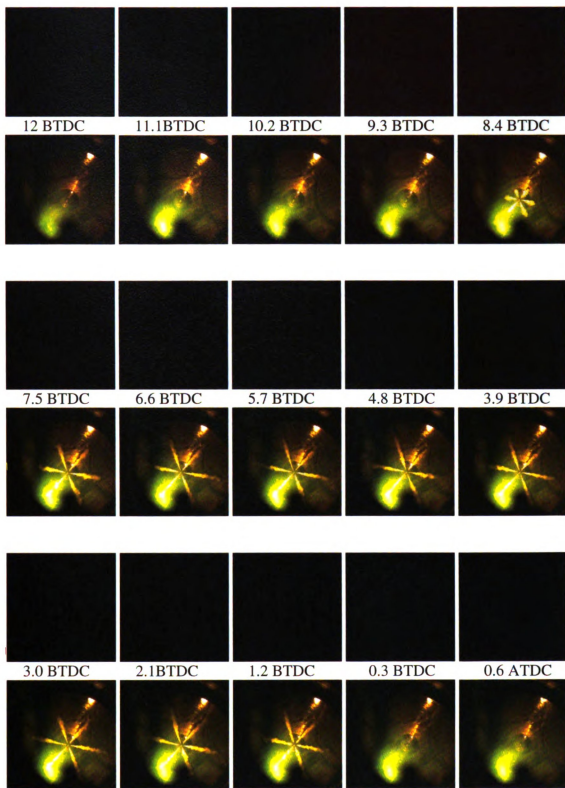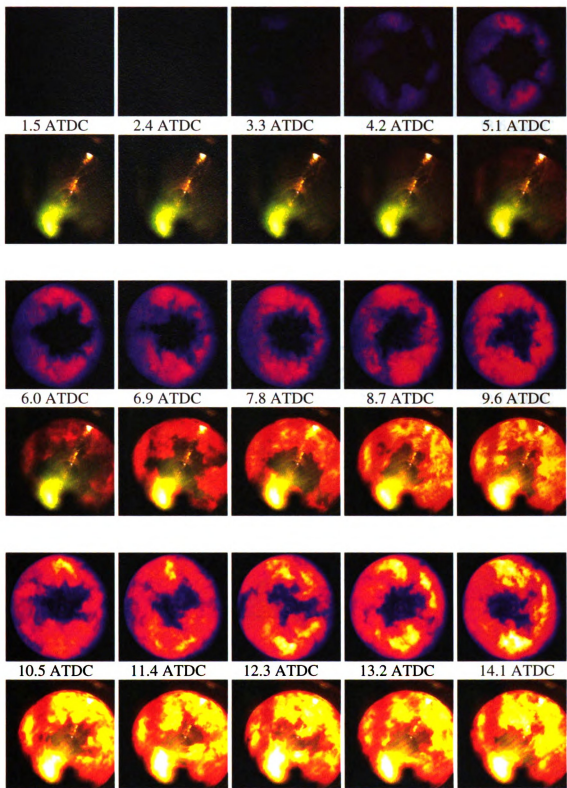## COMPOSITE CYCLE OF 6-HOLE NOZZLE, 0.63 PULSE WIDTH

Figure 34: Composite engine cycle at 0.9 CAD increments for 6-hole nozzle, 0.63ms pulse width case. The infrared images are above the CAD, high-speed images are below.

Figure 34 (continued): Composite engine cycle at 0.9 CAD increments for 6-hole nozzle, 0.63ms pulse width case. The infrared images are above the CAD, high-speed images are below.
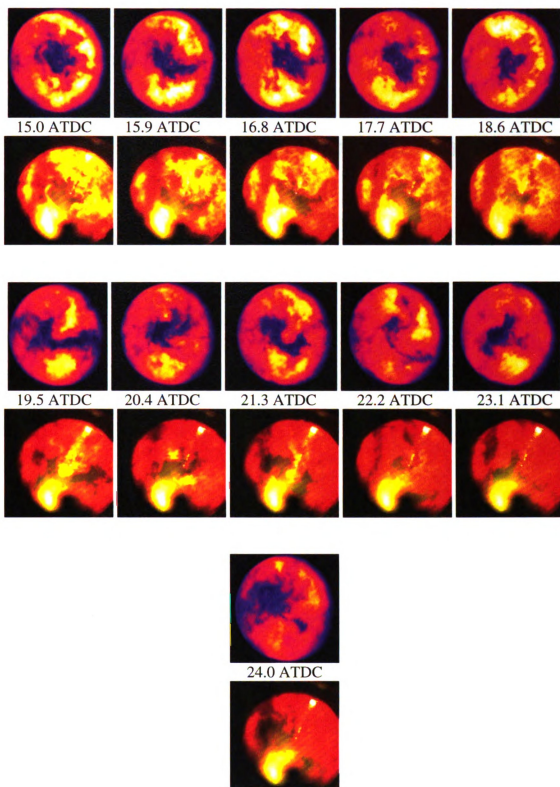
15.0 ATDC   15.9 ATDC   16.8 ATDC   17.7 ATDC   18.6 ATDC

19.5 ATDC   20.4 ATDC   21.3 ATDC   22.2 ATDC   23.1 ATDC

24.0 ATDC

Figure 34(continued): Composite engine cycle at 0.9 CAD increments for 6-hole nozzle, 0.63ms pulse width case. The infrared images are above the CAD, high-speed images are below.

APPENDIX E

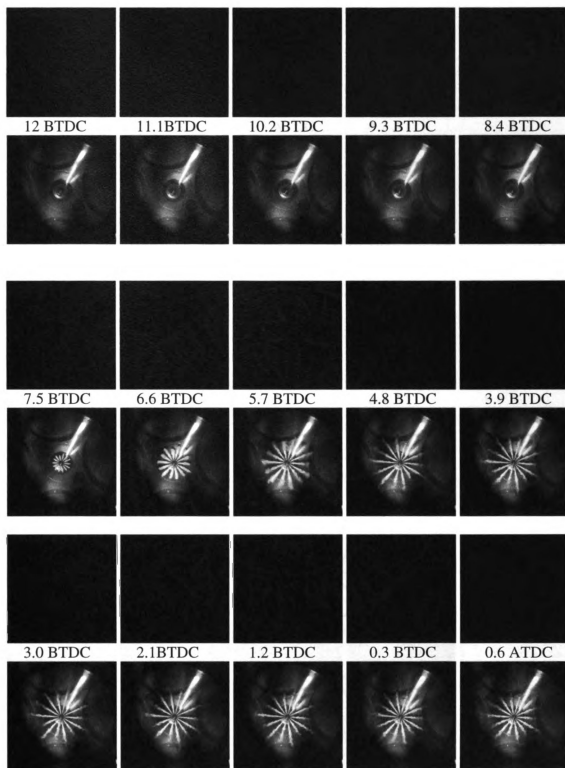## COMPOSITE CYCLE OF 7+7-HOLE NOZZLE, 0.82 PULSE WIDTH

Figure 35: Composite engine cycle at 0.9 CAD increments for 7+7-hole nozzle, 0.82ms pulse width case. The infrared images are above the CAD, high-speed images are below.
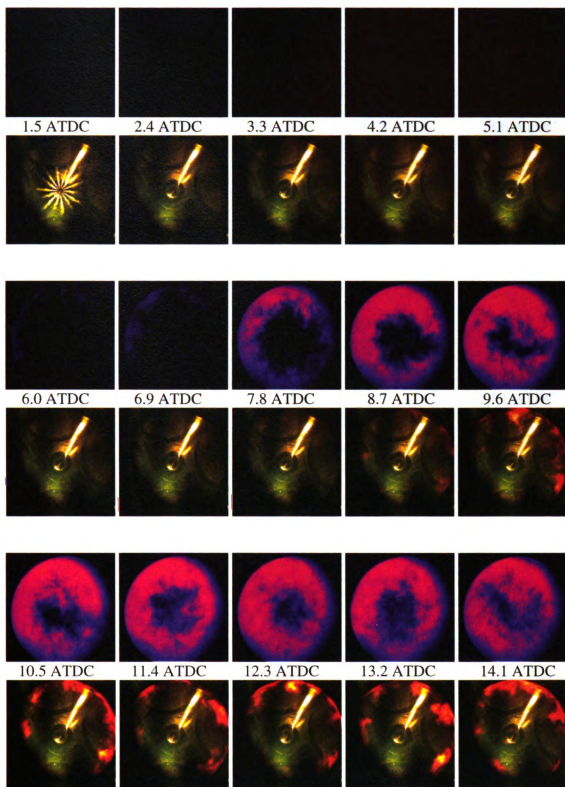
Figure 35 (continued): Composite engine cycle at 0.9 CAD increments for 7+7-hole nozzle, 0.82ms pulse width case. The infrared images are above the CAD, high-speed images are below.

15.0 ATDC   15.9 ATDC   16.8 ATDC   17.7 ATDC   18.6 ATDC

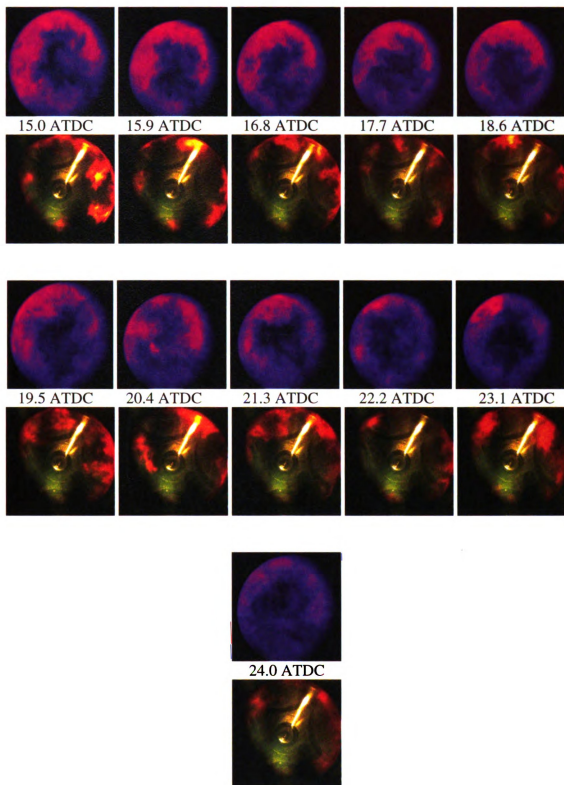19.5 ATDC   20.4 ATDC   21.3 ATDC   22.2 ATDC   23.1 ATDC

24.0 ATDC

Figure 35 (continued): Composite engine cycle at 0.9 CAD increments for 7+7-hole nozzle, 0.82ms pulse width case. The infrared images are above the CAD, high-speed images are below.

APPENDIX F

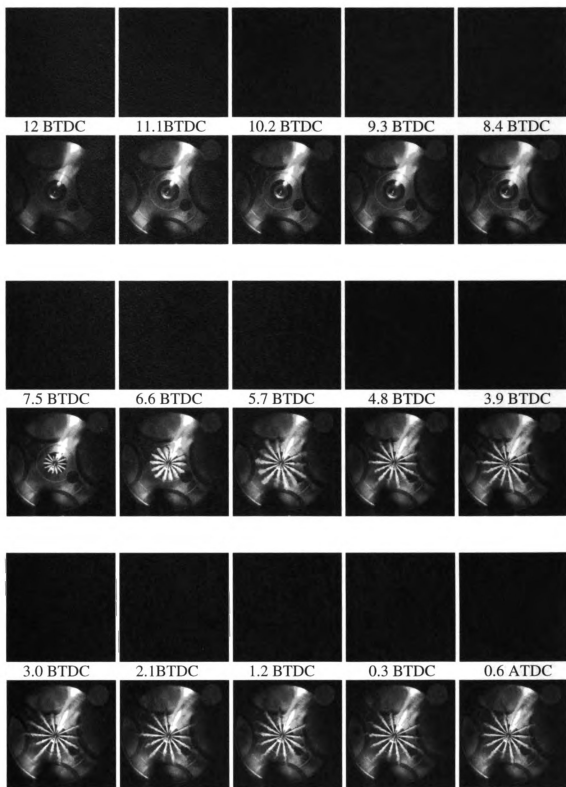## COMPOSITE CYCLE OF 14-HOLE NOZZLE, 1.00 PULSE WIDTH

Figure 36: Composite engine cycle at 0.9 CAD increments for 6-hole nozzle, 0.55ms pulse width case. The infrared images are above the CAD, high-speed images are below.

1.5 ATDC   2.4 ATDC   3.3 ATDC   4.2 ATDC   5.1 ATDC

6.0 ATDC   6.9 ATDC   7.8 ATDC   8.7 ATDC   9.6 ATDC

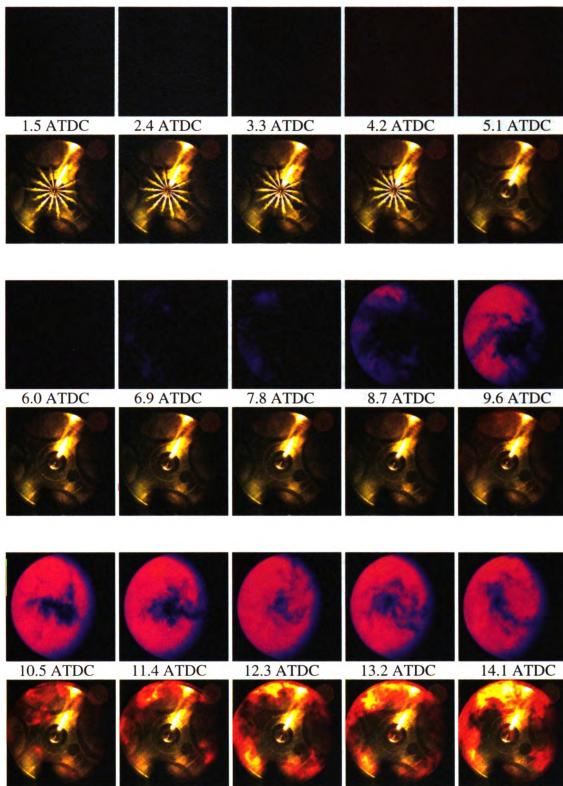10.5 ATDC   11.4 ATDC   12.3 ATDC   13.2 ATDC   14.1 ATDC

Figure 36 (continued): Composite engine cycle at 0.9 CAD increments for 6-hole nozzle, 0.55ms pulse width case. The infrared images are above the CAD, high-speed images are below.

15.0 ATDC	15.9 ATDC	16.8 ATDC	17.7 ATDC	18.6 ATDC

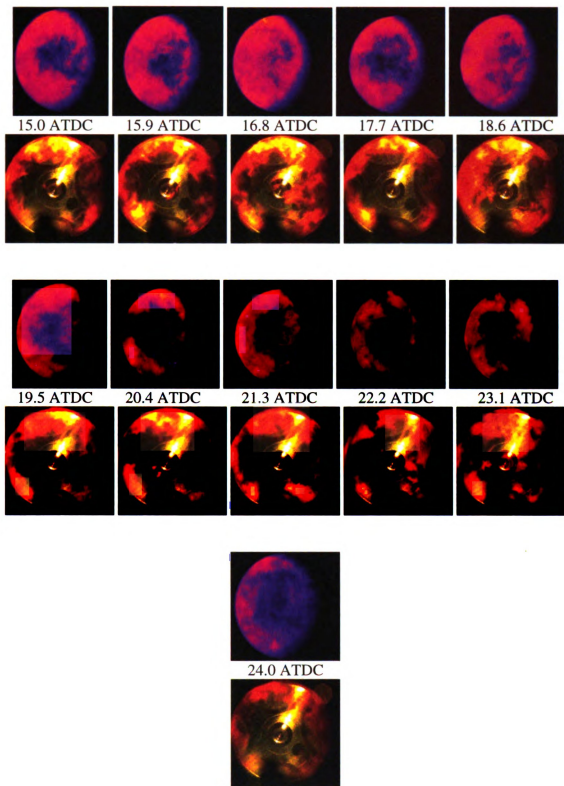|				
19.5 ATDC	20.4 ATDC	21.3 ATDC	22.2 ATDC	23.1 ATDC

24.0 ATDC

Figure 36 (continued): Composite engine cycle at 0.9 CAD increments for 6-hole nozzle, 0.55ms pulse width case. The infrared images are above the CAD, high-speed images are below.

APPENDIX G

HIGH-SPEED FRAMES OF MAXIMUM IMEP CYCLE - 6-HOLE NOZZLE, 0.63
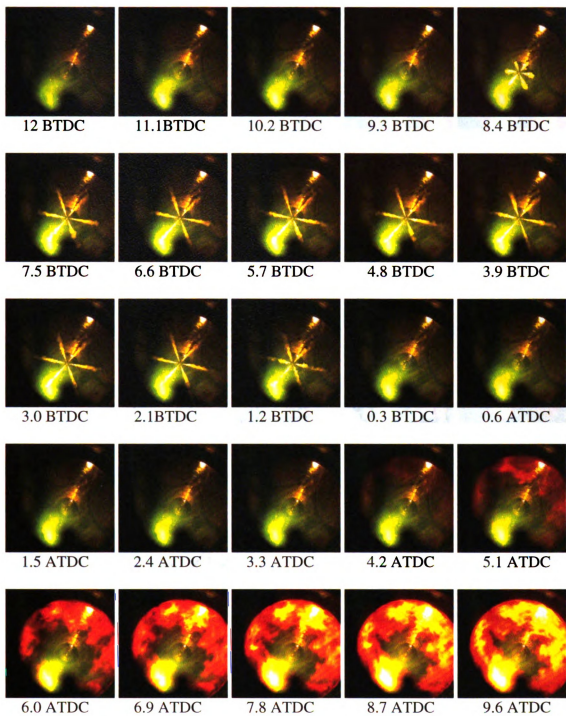
CASE

Figure 37: High-speed images of maximum IMEP cycle for 6-hole, 0.63 ms pulse width case.
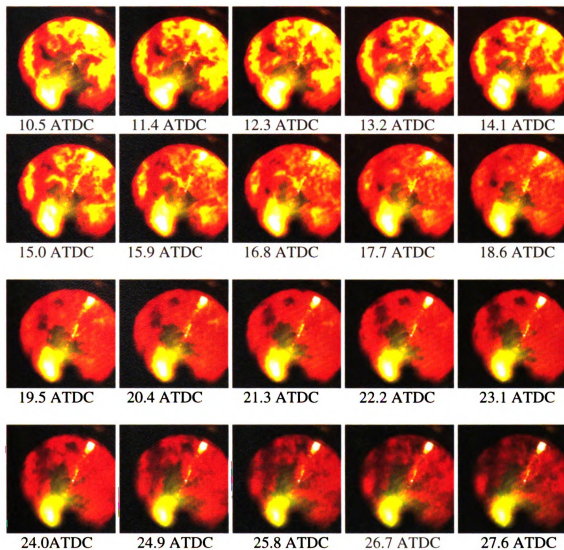
Figure 37 (continued): High-speed images of maximum IMEP cycle for 6-hole, 0.63 ms pulse width case.

APPENDIX H

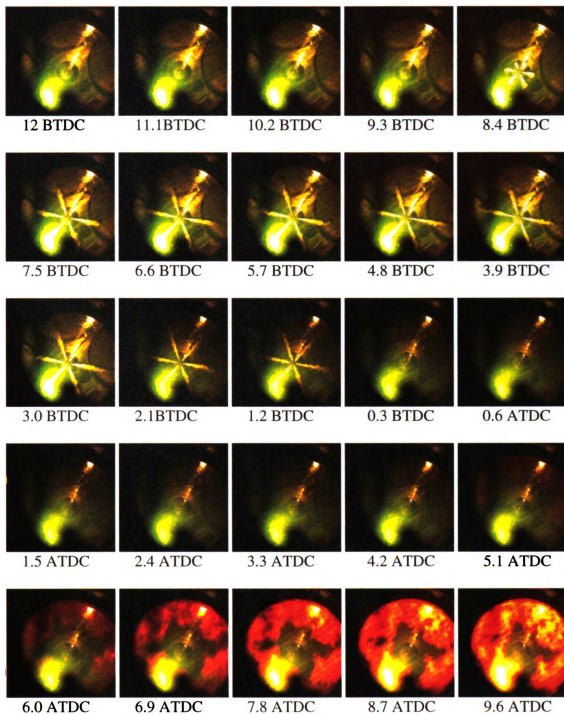## HIGH-SPEED FRAMES OF MINIMUM IMEP CYCLE

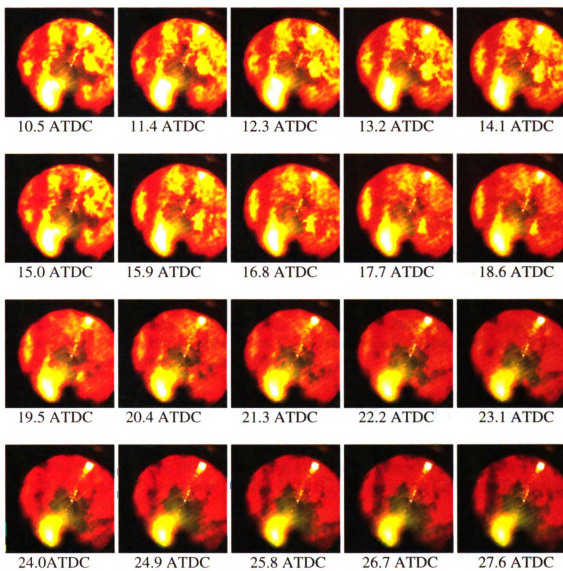Figure 38: High-speed images of minimum IMEP cycle for 6-hole, 0.63 ms pulse width case

Figure 38 (continued): High-speed images of minimum IMEP cycle for 6-hole, 0.63 ms pulse width case

REFERENCES

1.) Larsson, A., "Optical Studies in a Diesel Engine", 1999-01-3650, Society of Automotive Engineers Technical Paper Series, 1999

2.) Jansons, M., Lin, S., Rhee, K., "Infrared Spectral Analysis of Engine Preflame Emission", International Journal of Engine Research, Vol. 9, No. 3, pp 215-237, 2008

3.) Planas-Cuchi, E., Chatris, J., Lopez, C., Arnaldos, J., "Determination of Flame Emissivity in Hydrocarbon Pool Fires Using Infrared Thermography", Fire Technology, Vol. 39, pp 261-273, 2003

4.) Vollmer, M., Henke, S., Karstadt, D., Mollmann, K., Pinno, F., "Challenges in Infrared Imaging: Low Emissivities of Hot Gases, Metals and Metallic Cavities", 2004-07-27, Inframation 2004 Proceedings, 2004

5.) Tominaga, Y., Hiroshi, T., Strom, A., Uno, K., "Flame Temperature Measurement in Diesel Engine on Two Color Method Utilizing CMOS Camera", Journal of the Visualization Society of Japan, Vol. 25, pp 97-98, 2005

6.) Pickett, L., Siebers, D., "Non-sooting, Low Flame Temperature Mixing-Controlled DI Diesel Combustion", DEER 2003: 9th Diesel Engine Emissions Reduction Conference, Newport, RI, 2003

7.) Brahmi, L., Vietoris, T., Torero, J., Joulain, P., "Estimation of Boundary Layer Diffusion Flame Temperatures by Means of an Infrared Camera Under Microgravity Conditions", Measurement Science and Technology., Vol. 10, pp 859-865, 1999

8.) Brisley, P., Lu, G., Yan, Y., Cornwell, S., "Three Dimensional Measurement of Combustion Flames Using a Single Monochromatic CCD Camera", IEEE Transactions on Instrumentation and Measurement, Vol. 54, No. 4, pp 1417-1421, 2005

9.) Konishi, T., Ito, A., Saito, K., "Transient Infrared Temperature Measurements of Liquid-fuel Surfaces: Results of Studies of Flames Spread over Liquids", Applied Optics, Vol. 39, No. 24, pp 4278-4283, 2000

10.) Eastwood, P., Particulate Emissions from Vehicles, John Wiley and Sons, Hoboken, NJ, 2008

11.) Docquier, N., "Optical Investigation of the Effect of Fuel Jet Wall Impact Position on Soot Emissions in a Single Cylinder Common Rail Direct Injection Diesel Engine", 2002-01-0495, Society of Automotive Engineers Technical Paper Series, 2002

12.) Xu, G., Ikegami, M., Honma, S., Ikeda, K., Ma, X., Nagashi, H., Dietrich, D., Struk, P., "Inverse Influence of Initial Diameter on Droplet Burning Rate in Cold and Hot Ambiences: A thermal Action of Flame in Balance with Heat Loss", International Journal of Heat and Mass Transfer, Vol. 46, Issue 7, pp 1155-1169, 2003

13.) El-Shobokshy, M., "The Effect of Diesel Engine Load on Particulate Carbon Emission", Atmospheric Environment, Vol. 18, Issue 11, pp 2305-2311, 1984

14.) Huang, H., Zhang, Y., "Flame Colour Characterization in the Visible and Infrared Spectrum Using a Digital Camera and Image Processing", Measurement Science and Technology, Vol. 19, 2008

15.) Fettes, C., Schraml, S., Heimgartner, C., Leipertz, A., "Analysis of the Combustion Process in a Transparent Passenger Car DI-Diesel Engine by Means of a Multi-Dimensional Optical Measurement Technique", 2000-01-2860, Society of Automotive Engineers Technical Paper Series, 2000

16.) Van Basshuysen, R., Schafer, F., Internal Combustion Engine Handbook, SAE International, Warrendale, PA, 2004

17.) Pajot, O., Maunoury, B., Duverger, T., Mokaddem, K., Lacas, F., "Optical Investigation of Auto-Ignition Process in a Small DI Diesel Engine", 2002-01-1162, Society of Automotive Engineers Technical Paper Series, 2002

18.) Mittal, M., Zhu, G., Schock, H., Stuecken, T., Hung, D., "Burn Rate Analysis of an Ethanol-Gasoline, Dual Fueled, Spark Ignition Engine", 2008-66139, ASME, 2008

19.) Mittal, M., Zhu, G., Schock, H., "Fast Mass-Fraction Burned Calculation Using the Net Pressure Method for Real-time Applications", Journal of Automobile Engineering, Vol. 223, pp 389-394, 2008

20.) Turns, S., An Introduction to Combustion, 2nd Edition, McGraw Hill, Boston, MA, 2000

21.) Ma, Z., Huang, Z., Li, C., Wang, X., Miao, H., "Combustion and Emission Characteristics of a Diesel Engine Fueled with Diesel-Propane Blends", Fuel, Vol. 87, Issues 8-9, pp 1711-1717, 2008